



RESEARCH ARTICLE

10.1029/2023MS004192

Reducing Long-Standing Surface Ozone Overestimation in Earth System Modeling by High-Resolution Simulation and Dry Deposition Improvement

Key Points:

- A high-resolution Earth system model with interactive atmospheric chemistry is optimized on the Sunway high-performance computing system
- The updated ozone dry deposition velocity along with high-resolution simulations greatly reduces ozone overestimates across many regions
- We identify the mechanism that modulates differences in simulated ozone across different grid spacings in Earth system models

Supporting Information:

Supporting Information may be found in the online version of this article.

Correspondence to:

Y. Gao and S. Zhang,
yanggao@ouc.edu.cn;
szhang@ouc.edu.cn

Citation:

Gao, Y., Kou, W., Cheng, W., Guo, X., Qu, B., Wu, Y., et al. (2025). Reducing long-standing surface ozone overestimation in Earth system modeling by high-resolution simulation and dry deposition improvement. *Journal of Advances in Modeling Earth Systems*, 17, e2023MS004192. <https://doi.org/10.1029/2023MS004192>

Received 21 DEC 2023

Accepted 15 FEB 2025

Author Contributions:

Conceptualization: Yang Gao
Data curation: Shaoqing Zhang
Formal analysis: Yang Gao, Wenbin Kou
Investigation: Wenbin Kou
Methodology: Yang Gao
Resources: Jingshan Pan, Guangliang Liu, Xin Liu

Yang Gao¹ , Wenbin Kou¹, Wenxuan Cheng¹, Xiuwen Guo¹, Binglin Qu¹, Yubing Wu¹, Shaoqing Zhang² , Hong Liao³ , Deliang Chen^{4,5} , L. Ruby Leung⁶ , Oliver Wild⁷ , Junxi Zhang⁸, Guangxing Lin⁹ , Hang Su¹⁰, Yafang Cheng¹¹ , Ulrich Pöschl¹² , Andrea Pozzer^{13,14} , Leiming Zhang¹⁵, Jean-Francois Lamarque¹⁶ , Alex B. Guenther¹⁷ , Guy Brasseur¹⁸ , Zhao Liu¹⁹, Haitian Lu¹⁹, Chenlin Li¹⁹, Bin Zhao^{20,21} , Shuxiao Wang^{20,21} , Xin Huang²² , Jingshan Pan²³, Guangliang Liu²³ , Xin Liu²³, Haipeng Lin²⁴, Yuanhong Zhao²⁵ , Chun Zhao²⁶ , Junlei Meng²⁵, Xiaohong Yao¹ , Huiwang Gao¹ , and Lixin Wu²

¹Frontiers Science Center for Deep Ocean Multispheres and Earth System and Key Laboratory of Marine Environmental Science and Ecology, Ministry of Education, Ocean University of China, and Laoshan Laboratory, Qingdao, China, ²Frontiers Science Center for Deep Ocean Multispheres and Earth System, and Key Laboratory of Physical Oceanography, Ministry of Education, the College of Oceanic and Atmospheric Sciences, Ocean University of China, and Laoshan Laboratory, Qingdao, China, ³Jiangsu Key Laboratory of Atmospheric Environment Monitoring and Pollution Control, Jiangsu Engineering Technology Research Center of Environmental Cleaning Materials, Collaborative Innovation Center of Atmospheric Environment and Equipment Technology, School of Environmental Science and Engineering, Nanjing University of Information Science & Technology, Nanjing, China, ⁴Department of Earth System Sciences, Tsinghua University, Beijing, China, ⁵Department of Earth Sciences, University of Gothenburg, Gothenburg, Sweden, ⁶Atmospheric, Climate, and Earth Sciences Division, Pacific Northwest National Laboratory, Richland, WA, USA, ⁷Lancaster Environment Centre, Lancaster University, Lancaster, UK, ⁸Zhejiang Lab, Hangzhou, China, ⁹International Center for Climate and Environment Sciences, Institute of Atmospheric Physics, Chinese Academy of Sciences, Beijing, China, ¹⁰Key Laboratory of Atmospheric Environment and Extreme Meteorology, Institute of Atmospheric Physics, Chinese Academy of Sciences, Beijing, China, ¹¹Minerva Independent Research Group, Max Planck Institute for Chemistry, Mainz, Germany, ¹²Multiphase Chemistry Department, Max Planck Institute for Chemistry, Mainz, Germany, ¹³Atmospheric Chemistry Department, Max Planck Institute for Chemistry, Mainz, Germany, ¹⁴Climate and Atmosphere Research Center, The Cyprus Institute, Nicosia, Cyprus, ¹⁵Air Quality Research Division, Science and Technology Branch, Environment and Climate Change Canada, Toronto, ON, Canada, ¹⁶National Center for Atmospheric Research, Boulder, CO, USA, ¹⁷Department of Earth System Science, University of California Irvine, Irvine, CA, USA, ¹⁸Max Planck Institute for Meteorology, Hamburg, Germany, ¹⁹National Supercomputing Center in Wuxi, Wuxi, China, ²⁰State Key Joint Laboratory of Environment Simulation and Pollution Control, School of Environment, Tsinghua University, Beijing, China, ²¹State Environmental Protection Key Laboratory of Sources and Control of Air Pollution Complex, Beijing, China, ²²School of Atmospheric Sciences, Nanjing University, Nanjing, China, ²³Shandong Provincial Key Laboratory of Computer Networks, Qilu University of Technology (Shandong Academy of Sciences), Jinan, China, ²⁴John A. Paulson School of Engineering and Applied Sciences, Harvard University, Cambridge, MA, USA, ²⁵College of Oceanic and Atmospheric Sciences, Ocean University of China, Qingdao, China, ²⁶School of Earth and Space Sciences, University of Science and Technology of China, Hefei, China

Abstract The overestimation of surface ozone concentration in low-resolution global atmospheric chemistry and climate models has been a long-standing issue. We first update the ozone dry deposition scheme in both high- (0.25°) and low-resolution (1°) Community Earth System Model (CESM) version 1.3 runs, by adding the effects of leaf area index and correcting the sunlit and shaded fractions of stomatal resistances. With this update, 5-year-long summer simulations (2015–2019) using the low-resolution CESM still exhibit substantial ozone overestimation (by 6.0–16.2 ppbv) over the U.S., Europe, eastern China, and ozone pollution hotspots. The ozone dry deposition scheme is further improved by adjusting the leaf cuticle conductance, reducing the mean ozone bias by 19%, and increasing the model resolution further reduces the ozone overestimation by 43%. We elucidate the mechanism by which model grid spacing influences simulated ozone, revealing distinctive pathways in urban versus rural areas. In rural areas, grid spacing mainly affects daytime ozone levels, where additional NO_x emissions from nearby urban areas result in an ozone boost and overestimation in low-resolution simulations. In contrast, over urban areas, daytime ozone overestimation follows a similar mechanism due to the influence of volatile organic compounds from surrounding rural areas. However, nighttime ozone overestimation is closely linked to weakened NO titration owing to the redistribution of urban NO_x to rural areas. Additionally,

© 2025 The Author(s). Journal of Advances in Modeling Earth Systems published by Wiley Periodicals LLC on behalf of American Geophysical Union. This is an open access article under the terms of the [Creative Commons Attribution-NonCommercial-NoDerivs License](https://creativecommons.org/licenses/by/4.0/), which permits use and distribution in any medium, provided the original work is properly cited, the use is non-commercial and no modifications or adaptations are made.

Software: Wenbin Kou, Wenxuan Cheng, Xiuwen Guo, Binglin Qu, Yubing Wu, Junxi Zhang, Guangxing Lin, Zhao Liu, Haitian Lu, Chenlin Li, Haipeng Lin, Yuanhong Zhao, Chun Zhao, Junlei Meng

Supervision: Shaoqing Zhang, Lixin Wu

Validation: Leiming Zhang, Jean-Francois Lamarque

Writing – original draft: Yang Gao

Writing – review & editing: Hong Liao,

Deliang Chen, L. Ruby Leung, Oliver Wild, Hang Su, Yafang Cheng, Ulrich Pöschl, Andrea Pozzer, Alex B. Guenther, Guy Brasseur, Bin Zhao, Shuxiao Wang, Xin Huang, Xiaohong Yao, Huiwang Gao

stratosphere-troposphere exchange may also contribute to reducing ozone bias in high-resolution simulations, warranting further investigation. This optimized high-resolution CESM may enhance understanding of ozone formation mechanisms, sources, and changes in a warming climate.

Plain Language Summary Traditionally, low-resolution Earth system models have persistently overestimated surface ozone concentrations. Building on our previous optimization of the high-resolution Community Earth System Model version 1.3 for the Sunway heterogeneous-architecture high-performance computing system, we have enhanced both the efficiency and accuracy of high-resolution Earth system simulations with interactive atmospheric chemistry. This advancement enables a systematic evaluation of the benefits of high-resolution (~25 km atm) modeling compared to its low-resolution (~100 km atm) counterpart. Our findings show that while improving ozone sinks, such as ozone dry deposition velocity, can partially reduce bias in low-resolution simulations, increasing model resolution significantly mitigates ozone overestimation. Furthermore, we identify a key mechanism driving simulated ozone differences across grid spacings: the misrepresentation of urban and rural emission redistribution in low-resolution models alters the dominant ozone formation regimes controlled by volatile organic compounds and nitrogen oxides, leading to ozone biases. This newly optimized high-resolution CESM is expected to improve our understanding of ozone formation mechanisms, emission sources, and future changes in a warming climate.

1. Introduction

Climate and air quality interact strongly through multiple pathways (Fiore et al., 2015; Fu & Tian, 2019). Climate affects air quality by modulating photochemical reaction rates (Jacob & Winner, 2009), precursor emissions such as biogenic sources (Zhang et al., 2018), and sinks like water vapor, which facilitates ozone removal in remote areas (von Schneidmesser et al., 2015). Conversely, air pollutants exert substantial effects on climate. For example, solar ultraviolet radiation can be absorbed by gases, such as ozone, and be influenced by aerosols through direct radiative effects (Madronich, 1993; Thorsen et al., 2020). Aerosols can further act as cloud condensation nuclei and modify the properties of clouds (Huang et al., 2006; Quaas et al., 2009). Earth system models are key tools to understand these complex interactions, and increasing their spatial resolution is an important direction for enhancing such models, along with model process development and computational advancement (Stevens et al., 2023).

While the grid spacings of models that participated in the first phase of the Coupled Model Intercomparison Project ranged from 5.6° to 2.8° (Lambert & Boer, 2001), the resolutions of models that participated in CMIP5 and CMIP6 have increased notably to approximately 1°–3° (Ahmed et al., 2019). However, such resolutions remain too coarse to resolve heterogeneities in orography, emissions, land cover, and atmospheric processes, which together strongly affect chemical processes such as ozone formation regimes (Young et al., 2018).

Multi-model intercomparison projects aiming to address the interactions between chemistry and climate began with the Atmospheric Chemistry and Climate Model Intercomparison Project (ACCMIP; (Lamarque et al., 2013)), followed by the Chemistry–Climate Model Initiative (CCMI; (Morgenstern et al., 2017)) and the Aerosol Chemistry Model Intercomparison Project (AerChemMIP; (Collins et al., 2017)) endorsed by the CMIP6. As part of CMIP6, the High Resolution Model Intercomparison Project (HighResMIP) was established to pursue high-resolution simulations, though its primary focus remains on climate rather than atmospheric chemistry. The slow progress of high-resolution Earth system modeling in tackling chemistry–climate interactions is partly attributable to the much more intensive computational resources required to represent interactive atmospheric chemistry. Considering the importance of chemistry–climate interactions in affecting air quality, which has a strong impact on human health (Lelieveld et al., 2015) and climate processes such as the hydrological cycle (Ramanathan et al., 2001), it is imperative to develop high-resolution Earth system models suitable for delineating the complex processes involved in these interactions, and further enhance the understanding of how these processes may respond to a warming climate. While the scientific questions to be addressed in climate and air quality interactions are multi-faceted, we primarily focus on the gas phase air pollutant ozone in this study.

Ozone concentrations are closely associated with both precursor emissions and meteorological conditions (Wang et al., 2017). Precursors originate from both anthropogenic and natural sources. The large spatial heterogeneity of

anthropogenic emissions (Gao et al., 2022b; Zheng et al., 2021) can strongly affect the spatial distribution of ozone concentration (Forkel & Knoche, 2007; Markakis et al., 2014). Therefore, numerical simulations with coarse resolution cannot accurately resolve the spatial variability of ozone precursor emissions, which is one of the factors yielding large biases in ozone simulations and leading to the long-standing issue of ozone overestimation highlighted in the most recent Intergovernmental Panel on Climate Change assessment report (Liao et al., 2021; Szopa et al., 2021). For example, on the basis of the low-resolution ($1.9^\circ \times 2.5^\circ$) Community Earth System Model (CESM), the simulated maximum daily 8-hr average (MDA8) ozone concentrations, averaged in summer during the period 2001–2010 over the rural areas of Europe and the eastern U.S., are substantially overestimated (by >20 ppbv) at a number of observational sites (see Figure 8 in (Lamarque et al., 2012)). The overestimation of ozone in rural areas exhibited in the CESM is also commonly seen in other global models (Wild & Prather, 2006), and even in regional models at relatively low-resolution of $\sim 0.5^\circ$ (Li et al., 2019). For example, several studies based on five to seven CMIP6 models, including those in AerChemMIP, consistently show positive ozone biases year-round, in both rural areas over the land and oceanic regions, with monthly mean biases as high as 20 ppbv (Turnock et al., 2020; Zanis et al., 2022). In particular, the overestimation across the entire year over oceanic regions indicates that the ozone deposition velocity is likely too low, given the weak photochemistry in these environments (Clifton, Fiore, et al., 2020).

It has been suggested that the ozone bias can be caused by incorrect emission data and the incapability of low-resolution models to separate emissions between urban and rural areas (Lamarque et al., 2012; Shao et al., 2022). Specifically, NO_x emissions over rural areas are typically lower than those over urban areas with an opposite behavior for biogenically emitted organic compounds, and models with grid spacings of 1° or coarser will artificially distribute these emissions between the two areas. This may amplify NO_x emissions over rural areas, where ozone production efficiency tends to be higher than that in urban areas. In particular, over rural regions rich in isoprene, triggering a larger ozone increase compared with an urban area for the same additional amount of NO_x emissions (Kleinman, 2000; Liu et al., 1987; Sillman et al., 1990b). Moreover, emission projections depicted by coarse-scale grids may result in biases in future emissions; for example, the same emission projection factor for both urban and rural areas within one grid could lead to policy misclassification because the policies for urban and rural areas may be quite different (Lauwaet et al., 2014; Markakis et al., 2014, 2016).

The effect of accurately calculating ozone dry deposition has been considered as another important factor affecting ozone simulations, and this is subject to large uncertainties. The ozone dry deposition flux is determined by the dry deposition velocity and ozone concentration. Following the “resistance approach” suggested by Wesely (1989), ozone dry deposition velocity (V_d) is constrained by aerodynamic resistance (R_a), quasi-laminar sub-layer resistance (R_b), and canopy resistance (R_c) (Fowler et al., 2001; Wesely & Hicks, 2000). In areas with large amounts of vegetation, ozone dry deposition velocity is generally determined by canopy resistance or conductance ($\frac{1}{R_c}$). Underestimation of ozone dry deposition has been widely reported, leading to systematic overestimation of ozone (Hardacre et al., 2015; Val Martin et al., 2014). All 13 global models, with online calculation of dry deposition velocity, used in the Task Force on Hemispheric Transport of Air Pollution (HTAP) intercomparison (Hardacre et al., 2015) applied versions of the Wesely dry deposition scheme (Wesely, 1989). Their results showed substantial underestimation of ozone dry deposition in forest areas (see Figures 6 and 7 in Hardacre et al., 2015), especially for regions with high observed values; monthly mean simulated values were mostly below 0.4 cm s^{-1} , whereas the observed monthly mean ozone dry deposition velocities reached as high as $0.8\text{--}1.0 \text{ cm s}^{-1}$.

Using newly deployed heterogeneous Sunway supercomputers and the CESM, we have recently constructed a series of high-resolution simulations, referred to as SW-HRESMs, with spatial resolutions of the atmospheric and oceanic components ranging from $\sim 0.25^\circ$ to 0.05° and $0.1^\circ\text{--}0.03^\circ$, respectively (Zhang et al., 2020a, 2023). These high-resolution simulations exhibit greatly improved capability to simulate atmospheric blocking (Gao et al., 2025), downward solar radiation (Kou et al., 2023), sea surface temperature (Chang et al., 2020), and associated extremes, such as marine (Guo et al., 2022) and atmospheric heatwaves (Gao et al., 2023), which are closely associated with ozone formation through stimulating biogenic emissions and accelerating photochemistry (Gao et al., 2020; Kou et al., 2025). Based on the high-resolution ESM framework, this study conducts a comprehensive evaluation of the added value of high-resolution ESMs in simulating surface ozone concentrations, as well as identifying remaining issues which call for coordinated efforts by the community.

2. Methods

2.1. Model Setup and Evaluation of Meteorological Parameters

In this study, we used CESM1.3 with the same settings as several previous high-resolution modeling studies (Chang et al., 2020; Guo et al., 2022; Zhang et al., 2020a). Two spatial resolution configurations, a nominal 1° and 0.25° , were applied in Community Atmosphere Model 5.0 (CAM5) configured with the spectral element dynamical core, with prescribed sea surface temperature and sea ice at spatial resolutions of $1.0^\circ \times 1.0^\circ$. The parallelism optimization of the high-resolution ESM on a heterogeneous architecture supercomputing system is detailed in Section S1 in Supporting Information S1. The Model for Ozone And Related chemical Tracers (MOZART) was used as the gas phase chemistry mechanism, and the modal aerosol module with three lognormal modes (MAM3) was used as the aerosol scheme (Liu et al., 2012). No nudging was used in the atmospheric simulations in this study. Simulations were conducted over May, June, July, and August, representing summer in the Northern Hemisphere, over the period 2015–2019, with the month of May as a spin-up period. Prior to that, a half-year spin-up is applied, primarily for tropospheric ozone, considering that tropospheric ozone initially starts from zero. Stratospheric ozone is specified using climatological monthly averages at the upper boundary, derived from the period 1996 to 2005, as simulated by the Whole Atmosphere Community Climate Model (WACCM) during the evaluation of coupled chemistry-climate models (WACCM Ref1.4 CCMVal2; (Morgenstern et al., 2010)), with the zonal mean ozone distribution from ~ 400 hPa to 0.1 hPa (Figure S2 in Supporting Information S1). When examining stratospheric ozone variability, a linearized stratospheric ozone (Linoz; (Hsu & Prather, 2009)) approach may be applied for modeling stratospheric ozone chemistry. This method is utilized in models like the U.S. Department of Energy's (DOE) new Energy Exascale Earth System Model (E3SMv1; (Golaz et al., 2019)), which necessitates a longer spin-up period for accurate simulation.

The physics configuration in CAM5 selected in SW-HRESM is based on the setup in a previous study (Meehl et al., 2019). Model tuning was necessary for both low and high resolutions to achieve a top-of-atmosphere radiation balance, as detailed in Section 2.2 of Chang et al. (2020). The physics time step is half an hour (1,800 s) for the low-resolution (1°) simulations and 900 s for the high-resolution (0.25°) simulations. This setting aligns with the recommendation in Caldwell et al. (2019), which indicates that high-resolution simulations with approximately 16 times more grid points than low-resolution simulations generally require a time step that is two times shorter. This configuration in CAM5 includes several updates, such as transitioning from the Eulerian to the Lagrangian method for vertical advection, making minor adjustments to the microphysics and radiation schemes, and updating the heterogeneous freezing code and gravity wave parameterization, compared to earlier versions like CAM4. Meehl et al. (2019) demonstrated that these improvements in physics, whether at a 1° or 0.25° resolution, can significantly reduce the bias (by approximately 15%–20%) related to weakened storm track strength, as indicated by the maximum eddy kinetic energy at 850 hPa. Additionally, the study showed that with the same CAM5 physics, the 0.25° resolution further reduces the bias by 20% compared to the 1° resolution. The improvement in storm tracks is linked to an enhanced meridional SST gradient, driven by an increase in mid-latitude low clouds, which decreases incoming solar radiation and thus reduces midlatitude SSTs.

After conducting multi-century simulations using both high- and low-resolution configurations (Zhang et al., 2020a), Chang et al. (2020) performed the first comprehensive evaluation of mean climate and climate extremes using this data set. Their findings indicated that high-resolution simulations achieve improvements in key metrics such as global mean 2-m air temperature and sea-surface temperature, and tropical cyclone representation. Building on this work, we extended the analysis to focus on extreme weather events, including heat waves (Gao et al., 2023), extreme integrated water vapor transport events (atmospheric rivers) and the associated coastal extreme precipitation (Guo et al., 2024). These studies collectively demonstrate an improved capability of high-resolution simulations in reproducing climate extremes. Furthermore, we performed an uncentered spatial root mean square error (RMSE) analysis for several variables, including downward surface solar radiation, 2-m air temperature, daily precipitation, total cloud cover, and zonal wind at 800 hPa and 200 hPa (Table S2 in Supporting Information S1). The spatial distributions of total cloud cover and zonal wind are illustrated in Figure S3 in Supporting Information S1. The results reveal that the high-resolution model generally show lower RMSE values across most variables, with the exception of 200 hPa zonal wind, which enhances confidence in the accuracy of high-resolution simulations.

The deep convection scheme may not scale effectively with the increase in grid spacing. To evaluate how finer grid spacings may improve precipitation simulations, we analyze the large-scale and convective precipitation

Table 1
Descriptions of Different Dry Deposition Cases

Parameters	Cases			Model
	R_s	R_{lu} (wet condition)	R_{lu} (dry condition)	
LE20	Add LAI and modify R_s based on Equation 1			CESM-LR
LE20_Wet	Add LAI and modify R_s based on Equation 1	Modify R_{lu} initial condition and modify R_{lu} based on Equation 2		CESM-LR
LE20_WetDry	Add LAI and modify R_s based on Equation 1	Modify R_{lu} initial condition and modify R_{lu} based on Equation 2	Modify R_{lu} initial condition, normalized by relative humidity in the exponent form based on Equation 2	CESM-LR
LE20_Wet_SW-HRESM	Add LAI and modify R_s based on Equation 1	Modify R_{lu} initial condition and modify R_{lu} based on Equation 2		SW-HRESM

(Figures S4 and S5 in Supporting Information S1). While the zonal mean distribution of total precipitation (the sum of large-scale and convective components) is comparable between the high-resolution and low-resolution simulations, the high-resolution run shows a noticeably larger fraction of large-scale precipitation. This shift aligns more closely with reanalysis data from ERA5, suggesting improved realism in the high-resolution simulations. The increase in the large-scale component of precipitation is likely related to enhanced upper-level condensational heating and reduced lower-level evaporative cooling (Boyle & Klein, 2010), consistent with findings from previous studies (Bameister et al., 2014; Terai et al., 2018; Xie et al., 2018). The changes in the ratio of large-scale to total precipitation appear to be more strongly influenced by the increase in horizontal resolution, which enables the model to resolve a broader range of motion scales (Terai et al., 2018). Additionally, a reduction in time step can diminish the influence of convection parameterization (Williamson, 2013). However, the effect of time step may be marginal, considering that the time scales of deep and shallow convection are approximately 1 hr and 30 min, respectively. Given that the low-resolution simulations use a 30-min time step—comparable to these time scales—the effect of a smaller time step (15 min) in high-resolution runs might be less pronounced, as it falls below the time scales of both deep and shallow convection (Williamson, 2013).

2.2. Emissions

Anthropogenic emissions, including emissions from power plants, industry, residential, road and offroad transportation, solvents, agriculture, and shipping were obtained from CAMS-GLOB-ANT v4.2-R1.1 (<https://portal.aeris-data.fr/CAMS-GLOB-ANT>; (Granier et al., 2019)), herein referred to as CAMS. The CAMS emissions are at a monthly scale with a spatial resolution of $0.1^\circ \times 0.1^\circ$, and emissions over China are updated using the Multi-resolution Emission Inventory for China (MEIC) (Li et al., 2017) to improve accuracy. The gas phase emission mapping was similar to the method introduced in Schwantes et al. (2022), whereas the aerosol emission mapping was based on Liu et al. (2012). The anthropogenic emission sectors of power plants and industry are vertically distributed to the altitude as high as 300 m based on Table 1 in Dentener et al. (2006).

Biomass burning emissions were provided by the Fire INventory from National Center for Atmospheric Research (FINN; (Wiedinmyer & Emmons, 2022)), with a high spatial resolution of 0.1° . The recently released FINN version 2.5 was used (<https://rda.ucar.edu/datasets/ds312-9>; (Wiedinmyer et al., 2023)), which includes small-scale fire emission data based on active fire products from both the Moderate Resolution Imaging Spectroradiometer (MODIS) and Visible Infrared Imaging Radiometer Suite (VIIRS; Tang et al., 2022). The raw text files at ~ 1 km were gridded into NetCDF format at 0.1° , and emissions of primary aerosols and their precursors were distributed over a number of vertical layers according to the injection heights as in Dentener et al. (2006), similar to the methodology applied in our previous studies (Chen et al., 2023; Guan et al., 2020). VIIRS enhances the capability of detecting small fires (Chen et al., 2023; Wiedinmyer et al., 2011; Zhang et al., 2020b), which are generally undetected by the MODIS product. Volcanic and marine emissions (mainly dimethyl sulfide) were obtained from the Aerosol Inter Comparison Project (AeroCom; (Dentener et al., 2006)). Aircraft emissions were derived from the Community Emissions Data System (Hoesly et al., 2018). Biogenic volatile organic compounds were generated online by the Model of Emissions of Gases and Aerosols from Nature version 2.1 (MEGAN2.1; (Guenther et al., 2012)).

The emissions at 0.1° resolution were directly used in the high-resolution simulations, whereas for the low-resolution simulations, the emissions were aggregated from 0.1° to $\sim 1.0^\circ$ resolution. For the high-resolution run at 0.25° , linear interpolation is performed in the model from 0.1° to 0.25° . While this interpolation method is not area-conservative, it does not significantly affect the overall magnitude. Using NO emissions from anthropogenic and biomass burning source as an example, the total global emissions based on 0.1° grid is 6.72 Tg per month during the summer of 2015–2019, and linear interpolation to either $\sim 0.25^\circ$ or $\sim 1.0^\circ$ grids yielding a difference within 1%.

2.3. Observational Data

Hourly ozone observational data for the U.S. were obtained from the Air Quality System (AQS, <https://www.epa.gov/aqs>; last access: 30 June 2022) and the Clean Air Status and Trends Network (CASTNET, <https://www.epa.gov/castnet>; last access: 30 April 2022). Observed hourly surface ozone concentrations in Europe and China were obtained from the European Monitoring and Evaluation Program (EMEP) database (<http://ebas.nilu.no>; last access: 30 January 2022) and the China National Environmental Monitoring Center (CNEMC; <http://www.pm25.in>, last access: 23 May 2021), respectively. Ozone dry deposition fluxes were obtained from CASTNET (last access: 30 April 2022). Additional surface ozone observations were sourced from the Tropospheric Ozone Assessment Report (TOAR) database (Fleming et al., 2018; Mills et al., 2018). Ozone Profiles with ozonesondes were obtained from the Global Monitoring Laboratory of National Oceanic and Atmospheric Administration Earth System Research Laboratories (<https://gml.noaa.gov/obop/mlo/programs/esrl/ozonesondes/ozonesondes.html>; last access: 30 January 2023). Note that the ozone observation data used in the main manuscript are from AQS, CASTNET, EMEP and CNEMC, with the spatial distributions of sites shown in Figure S6 in Supporting Information S1. The TOAR data set (site locations shown in Figure S7 in Supporting Information S1) includes the number of stations in urban, suburban, and rural areas, as shown in Table S3 in Supporting Information S1. Ozone vertical profiles are used in the supplementary information.

3. Results

3.1. Evaluation of Ozone Dry Deposition Velocity and Ozone Diurnal Cycle

Using the CESM at grid spacings of $1.9^\circ \times 2.5^\circ$, simulated MDA8 ozone concentrations, averaged over rural areas of Europe and the eastern U.S. during summer in the period 2001–2010, exhibited a pronounced overestimation, reaching >20 ppbv at a number of locations (Lamarque et al., 2012). In a subsequent study, Val Martin et al. (2014) determined that this overestimation was largely due to a substantial underestimation (by approximately 50%) of daily stomatal conductance, based on observed ozone dry deposition velocity. This underestimation led to a lower ozone dry deposition velocity and a systematic ozone overestimation, yielding a weighted summer ozone bias of 44% in the eastern U.S. They hypothesized that the Wesley scheme used in the CESM is overly simplistic, as it represents stomatal conductance—defined as the inverse of stomatal resistance (R_s)—as a function of only downward surface solar radiation and near surface air temperature, while neglecting the effects of canopy depth and leaf area index (Baldocchi et al., 1987; Fowler et al., 2009; Gao & Wesely, 1995). By adopting the Ball–Berry scheme (Collatz et al., 1991, 1992; Sellers et al., 1996), which relates stomatal resistance directly to the net leaf photosynthesis and integrates stomatal resistance based on the leaf area index over the canopy depth for sunlit and shaded leaves, Val Martin et al. (2014) showed that the underestimation of ozone dry deposition velocity could be slightly reduced, but the rate still remained too low. To further address this issue, they artificially increased the stomatal conductance by a factor of five, which evidently increased the ozone dry deposition velocity, thereby lowering ozone concentrations and reducing ozone overestimation. Nevertheless, this adjustment was based on an empirical scaling factor with large uncertainties, reflecting the complexities of the processes controlling ozone concentrations.

More recently, Emmons et al. (2020), referred to herein as LE20, pointed out an error in Val Martin et al. (2014) related to the summation of sunlit and shaded fractions of the stomatal resistances, noting that the sum should be performed in parallel (Equation 1) instead of in series. However, even after this error correction, the simulated ozone concentrations in LE20 remain overestimated (by an average of 13 ppbv in summer in the southeastern U.S.), and the lack of evaluation of the ozone dry deposition velocity makes it difficult to judge the effectiveness of the revised formula.

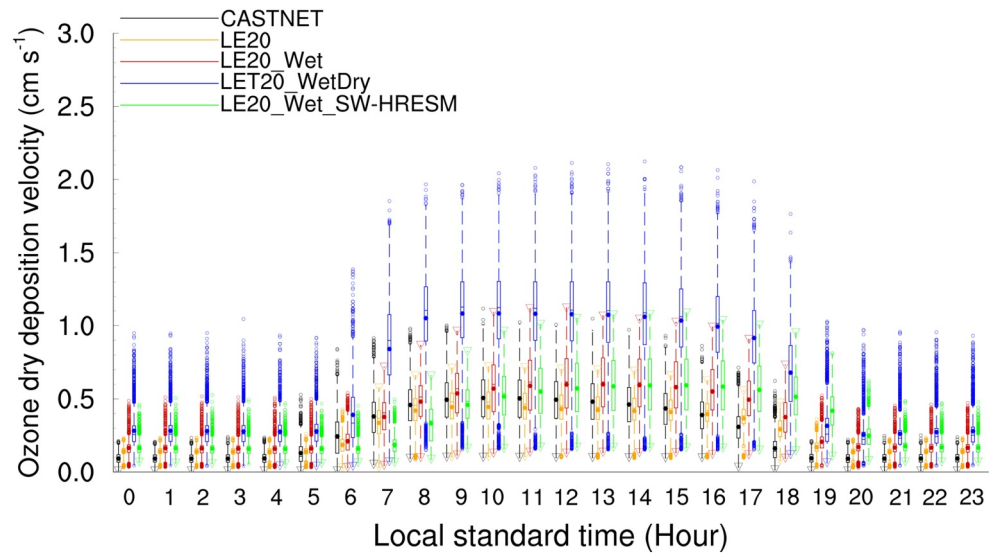


Figure 1. Box-and-whisker plot of the diurnal cycle (local standard time) of ozone dry deposition velocity. Shown are results in the U.S. for observations from CASTNET (black) and simulations based on the CESM-LR (orange, red, blue) from three scenarios as well as SW-HRESM based on LE20_Wet (green) described in Section 3.1 of the main text, with the 25th and 75th percentiles (boxes, and differences between 75th and 25th percentiles considered as interquartile ranges), medians (horizontal lines), averages (solid points), and line end points indicating values 1.5 times the interquartile range above the upper quartile and below the lower quartile. All other values are considered outliers and marked by hollow circles. For those without outliers, a triangle is added over the line end point. Note that all box-and-whisker plots in subsequent figures are drawn based on the same method. The simulation period covers the summers of 2015–2019, whereas 10 years of summers (2006–2015) from CASTNET are applied considering that CASTNET data are available prior to 2015. A multi-year average on each day was taken prior to drawing the plot; hence, the spread in the box-and-whisker plot indicates daily and spatial variabilities.

$$\frac{1}{R_s} = f_{\text{sun}} \times \text{LAI} \times \left(\frac{1}{r_s^{\text{sun}}} \right) + (1 - f_{\text{sun}}) \times \text{LAI} \times \left(\frac{1}{r_s^{\text{sha}}} \right) \quad (1)$$

where, f_{sun} and $1 - f_{\text{sun}}$ represent the fractions of sunlit and shaded leaves, respectively, and r_s^{sun} and r_s^{sha} indicate the stomatal resistance for the sunlit and shaded leaves, respectively.

For a systematic evaluation of ozone dry deposition velocities, the simulations in this study do not apply meteorological nudging, which are not amenable to a day-to-day comparison. Therefore, we compared the diurnal cycle of ozone dry deposition velocity over the U.S. during the summer simulation period of 2015–2019 with observations from CASTNET (shown in black in Figure 1). The dry deposition velocity in CASTNET is not directly measured, but is instead calculated using modeled dry deposition velocities from the Multilayer Model (Finkelstein et al., 2000; Meyers et al., 1998) and measured atmospheric concentrations (Schwede et al., 2011). We first applied the same dry deposition scheme and settings as those used in LE20 for the low-resolution simulations based on CESM-LR, with the diurnal cycle of simulated ozone dry deposition velocity shown in orange in Figure 1. In addition to stomatal conductance, leaf cuticle conductance ($\frac{1}{R_{lc}}$) in Equation 2 plays an important role in ozone dry deposition. In particular, the leaf cuticle conductance is closely associated with atmospheric humidity; for example, high humidity under dew point and rainfall, defined as daily precipitation < 1 mm, could greatly enhance O_3 uptake by leaf cuticles (Padro, 1996; Zhang et al., 2002, 2003). The initial condition of leaf cuticle resistance (R_{lc0}) during wet conditions in LE20 based on the Wesley scheme is considered too high, and smaller values have been suggested in Zhang et al. (2003); these were applied in this study to adjust the initial leaf cuticle resistance and the corresponding CESM-LR simulation scenario is referred to as LE20_Wet. The corresponding simulated ozone dry deposition velocity is shown in red in Figure 1. Meanwhile, for other days under dry conditions without dew or rainfall, the initial condition was adjusted to take the smaller value listed in Zhang et al. (2003), relative to the default value in CESM, and a normalization of

relative humidity in the exponent form was applied; the corresponding CESM-LR simulation scenario is referred to as LE20_WetDry. Information on these three cases is summarized in Table 1.

$$R_{lu} = \frac{R_{lu0}}{LAI} + RT, \quad (2)$$

where, R_{lu} is the leaf cuticle resistance, R_{lu0} is the initial leaf cuticle resistance, LAI is the leaf area index, and RT is a function of the 2-m air temperature, defined as $1,000 \times \exp(-T - 4)$, with T in units of Celsius.

As shown in Figure 1, the mean daytime (i.e., 9:00–15:00) ozone dry deposition velocity in the U.S. was 0.46 cm s^{-1} according to CASTNET, and 0.43 , 0.56 , and 1.04 cm s^{-1} for the three CESM-LR simulation scenarios: LE20, LE20_Wet, and LE20_WetDry. The ozone dry deposition velocity in LE20 was lower than that of CASTNET, whereas the other two scenarios gave higher values. The CASTNET ozone dry deposition velocity is based on a multi-layer model used in Meyers et al. (1998). Wu et al. (2018) compared five dry deposition schemes for calculating ozone dry deposition velocity over a temperate mixed forest in southern Ontario, Canada, using a 5-year observed flux database during the period May 2008 to April 2013 for evaluation. They found that the ozone dry deposition velocity based on the multi-layer model was, in general, a factor of one to two smaller than that of the other four schemes, and only one-third to half of the observed values (hourly values ranging from 0.3 to 1.0 cm s^{-1}). Similarly, Finkelstein et al. (2000) showed that the mean daytime ozone deposition velocity was 0.75 cm s^{-1} at a deciduous forest site (41.60°N , 78.77°W) in northwestern Pennsylvania, U.S. from April to October 1997.

A number of observations from literature is summarized in Clifton, Fiore, et al. (2020), and we select one reference (Li et al., 2018) within the simulation period of this study for comparison. They did field measurements at Ramat Hanadiv Nature Park near the Eastern Mediterranean coast during the summers of 2015 and 2016, showing ozone dry deposition of 0.39 cm s^{-1} and 0.31 cm s^{-1} on average during daytime and nighttime, respectively. The corresponding values based on LE20_wet is 0.28 cm s^{-1} and 0.18 cm s^{-1} in CESM-LR, indicating comparable results with observations but may underestimate ozone dry deposition. If LE20_WetDry is applied, the mean value at the grid of Ramat Hanadiv Nature Park is 0.52 cm s^{-1} , which is apparently too high. The overestimation of ozone dry deposition velocity in the method of LE20_WetDry is partly due to the lack of consideration of friction velocity. The friction velocity could be another important factor affecting the daily variability of ozone dry deposition velocity (El-Madany et al., 2017; Fares et al., 2014); in particular, the nighttime friction velocity may be much smaller than one (Zhang et al., 2003), so a normalization by friction velocity could be applied to increase the stomatal resistance and reduce the deposition velocity.

The simulated mean ozone concentrations using CESM-LR based on the three aforementioned deposition schemes over the U.S., southeastern U.S. (SEUS), Europe, and eastern China are shown in Figure 2. Based on LE20, the simulations successfully captured the diurnal cycles of ozone, but with ozone concentrations that were too high. Over the U.S., adjusting the leaf cuticle resistance during wet days (LE20_WET), mean ozone concentrations were slightly reduced (by 6%; 2.7 ppbv). Further adjusting the leaf cuticle resistance during dry days substantially reduced the ozone concentrations (by 6.7 ppbv), giving a mean value of 37.9 ppbv, which is much closer to the observations (32.5 ppbv). However, as illustrated in Figure 1, the ozone dry deposition in LE20_WetDry may be too high; hence, in the analysis below, LE20_Wet is selected as the optimal scheme for both low-resolution and high-resolution ESM simulations. For comparison, the ozone dry deposition based on the LE20_Wet method from the high-resolution model (SW-HRESM) is shown in Figure 1 (green), which is comparable to the daily mean dry deposition from the low-resolution CESM-LR LE20_Wet method, both being 0.35 . It must be noted that the ozone dry deposition scheme needs to be further improved and validated in future studies. The importance of ozone dry deposition on ozone concentration simulations can be inferred based on the following phenomenon. A previous assessment of Geophysical Fluid Dynamics Laboratory model shows it relatively well captures monthly variations of ozone dry deposition (Clifton, Paulot, et al., 2020), and this model corresponds to be one of the models with smallest ozone overestimate (Figure 4 in (Turnock et al., 2020)).

3.2. Evaluation of Ozone Concentrations Based on High- and Low-Resolution ESMs

After the evaluation of ozone dry deposition schemes, simulations were conducted during the summers of 2015–2019 using LE20_Wet at both high-resolution (SW-HRESM) and low-resolution (CESM-LR). The spatial

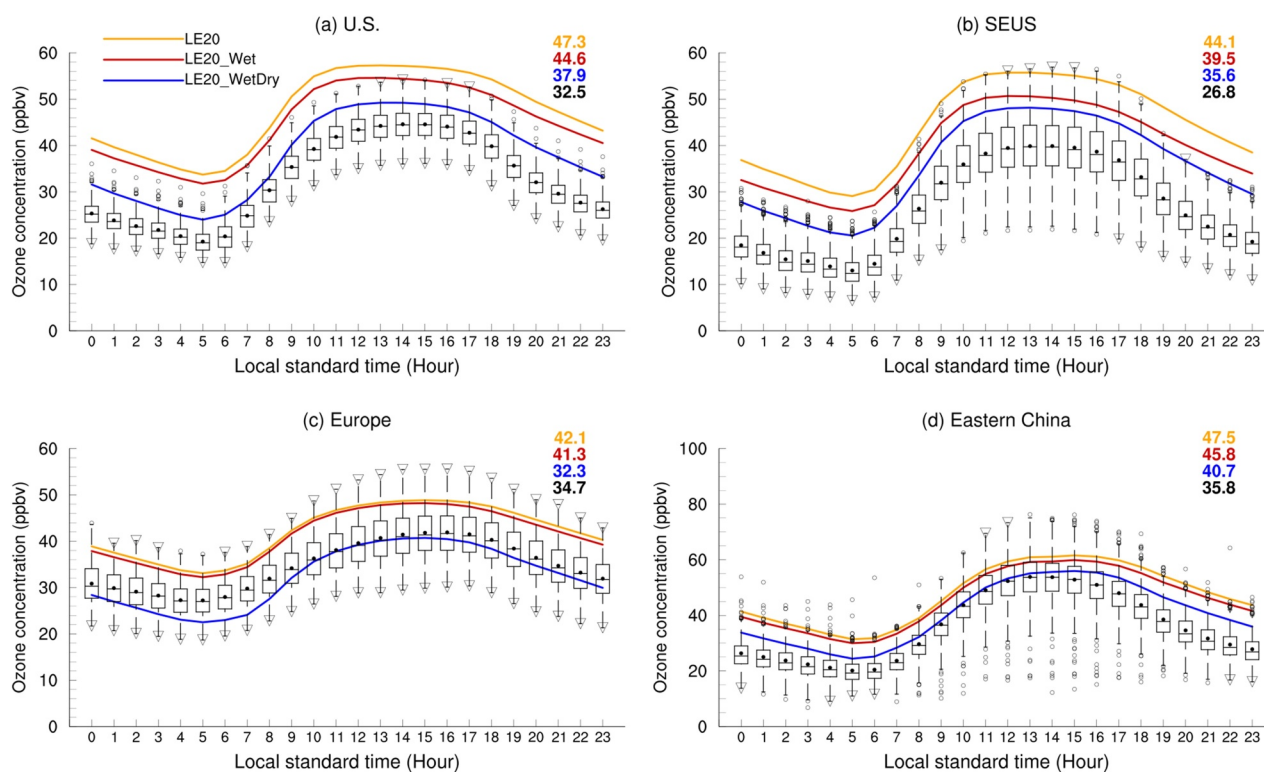


Figure 2. Box-and-whisker plots of regional mean diurnal cycles (local standard time) of ozone concentrations. Shown are results over the U.S. (a), Southeastern U.S. (SEUS; b), Europe (c) and Eastern China (d) during the summers of 2015–2019, with black lines and text representing observed values (observations sites shown in Figure S6 in Supporting Information S1), and colored lines and text indicating simulated results based on different ozone dry deposition schemes (LE20, LE20_Wet, and LE20_WetDry) using the CESM-LR.

distributions of surface MDA8 ozone concentrations over land areas in the Northern Hemisphere are displayed in Figure 3, with observations mainly covering the U.S., Europe, and China. The mean MDA8 ozone concentrations calculated over the observed grids were 44.4, 51.4, and 53.1 ppbv, based on observations, SW-HRESM, and CESM-LR, respectively. The observations showed hot spots over the western and southeastern U.S., northern China (including Beijing–Tianjin–Hebei (BTH) and the junction of Jiangsu, Anhui, Shandong, and Henan (referred to as SWLY)), mid-China (including the Yangtze River Delta (YRD)), and southern China (including the Pearl River Delta (PRD)). The high-resolution simulations (SW-HRESM) captured these hot spots relatively well, whereas the low-resolution simulations (CESM-LR) exhibited much weaker spatial heterogeneities and tended to show surface ozone concentrations that were too high. Further evaluation of the vertical profile of ozone from surface to ~20 km is conducted at eight sites (Figure S8 in Supporting Information S1), showing that both models in general capture well the vertical distribution of ozone, and for majority of sites, slightly lower mean bias from surface to 20 km is achieved in SW-HRESM compared to CESM-LR.

Additionally, an ozone budget analysis for tropospheric ozone, defined as ozone concentrations less than or equal to 150 ppbv (Prather et al., 2011; Young et al., 2013), is carried out (Table 2), revealing comparable ozone burden, ozone production, loss, dry deposition and stratosphere-troposphere exchange (STE) between SW-HRESM and CESM-LR. The budget is generally comparable to previous studies (e.g., Table 9 in (Lamarque et al., 2012)). Note that both STE and deposition play equally important roles in altering the summertime tropospheric ozone budget across the high- and low-resolution model simulations (Table 2). Given that it takes several weeks for ozone from STE to reach the surface from the upper troposphere, and considering that STE ozone flux peaks in late spring (e.g., Figure 7 of Hsu & Prather, 2009), STE might play an important role in influencing surface ozone levels during the summer months. The impact of STE on surface ozone in the high-resolution model still requires further investigation in future studies. Lightning flash rates and intensity are influenced by cloud top height (Price et al., 1997; Price & Rind, 1992), with additional details provided in Emmons et al. (2010). In summer, the magnitude of lightning-induced NO_x is 1.0 Tg N in the high-resolution simulation and 1.4 Tg N in the low-

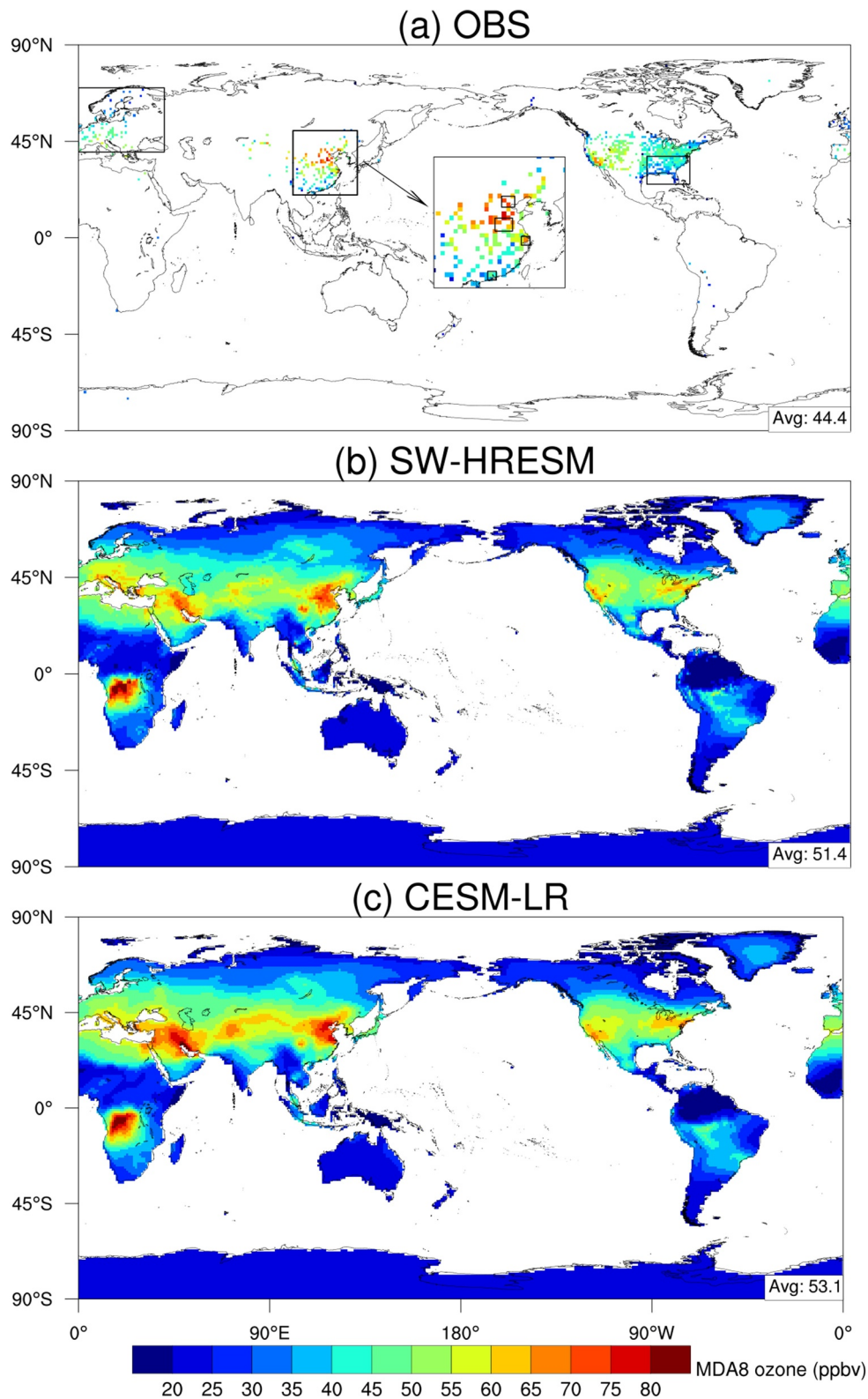


Figure 3. Spatial distributions of MDA8 ozone concentrations during the summers of 2015–2019. Shown are results based on (a) Observations, (b) SW-HRESM and (c) CESM-LR. The black squares show the areas of Europe, southeastern U.S. and four regions in China; from north to south, these are Beijing–Tianjin–Hebei, the junction of Jiangsu, Anhui, Shandong, and Henan, the Yangtze River Delta, and the Pearl River Delta. The mean MDA8 ozone value over the observational grids is shown in the top left of each panel. All simulations are presented at 1°.

Table 2
Tropospheric (Ozone <150 ppbv) Ozone Budget in Summer 2015

Name (units)	Models						
	Burden Tg	Production Tg summer ⁻¹	Loss Tg summer ⁻¹	Net chem. Tg summer ⁻¹	Deposition Tg summer ⁻¹	STE Tg summer ⁻¹	Lightning NO TgN summer ⁻¹
SW-HRESM	294	1,130	1,002	127	216	89	1.0
CESM-LR	312	1,131	1,004	128	232	104	1.4

resolution simulation (Table 2). As resolution increases, convective activity diminishes, as evidenced by reduced convective precipitation (Figures S4 and S5 in Supporting Information S1), leading to a reduction in lightning-produced NO_x compared to low-resolution simulations. When scaling summer lightning NO to an annual basis, these estimates likely align with current literature values (3–7 Tg N/year; (Khodayari et al., 2018)). Further evaluation of lightning NO is crucial to reduce uncertainties in its magnitude and its impact on ozone production.

To further evaluate ozone concentrations over major ozone pollution regions, including the U.S., Europe, and eastern China, as well as specific regions of the SEUS and metropolitan areas in China such as BTH, YRD, SWLY, and PRD, box-and-whisker plots of MDA8 ozone were constructed (Figure 4). Besides the observations, three simulation scenarios are displayed in Figure 4; these include two sets of low-resolution simulations with different ozone dry deposition schemes (the abovementioned LE20 and LE20_Wet schemes) referred to as CESM-LE20 and CESM-LR, respectively, and a high-resolution simulation with the LE20_Wet scheme (SW-HRESM). The CESM-LE20 is considered the base simulation. NO emissions from anthropogenic and biomass burning source over the eight areas at 0.1°, 0.25° and 1° are shown in Table S4 in Supporting Information S1. When comparing emission magnitude, the difference between 0.1° and 0.25° resolutions is minimal, and the comparison between 1° and 0.25° resolutions is also similar at the national level. However, at the regional level, the results for the lower resolution tend to be slightly higher, possibly due to edge effects in emission-dense areas,

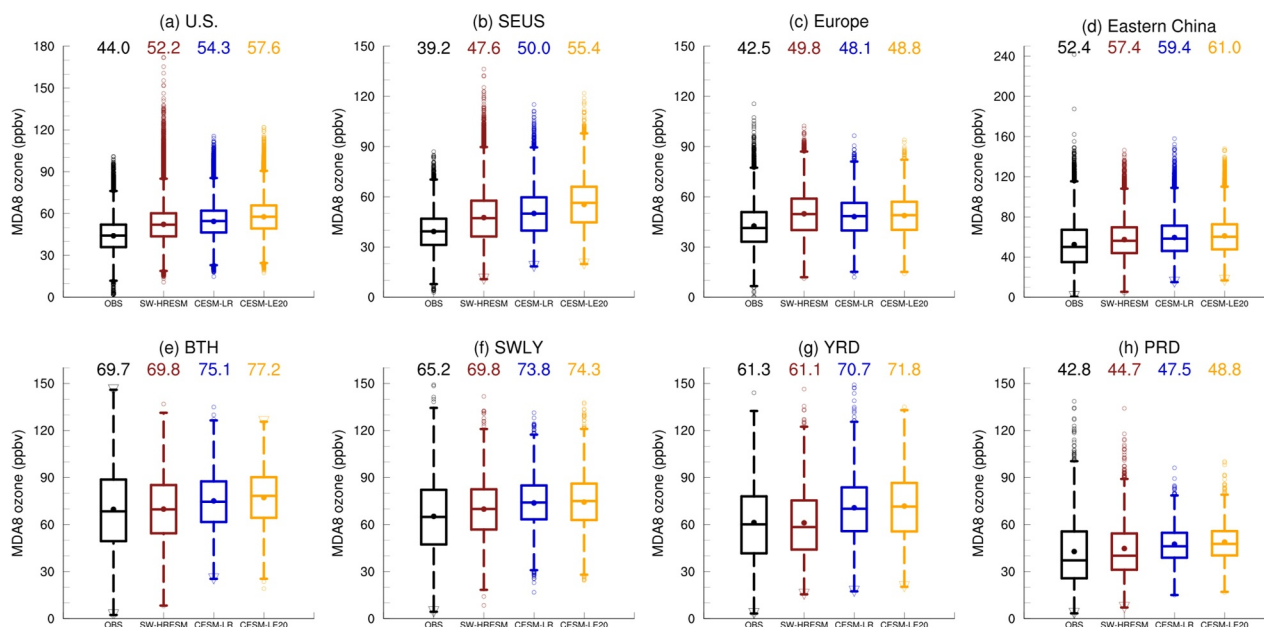


Figure 4. Box-and-whisker plots of MDA8 ozone during the summers of 2015–2019. Shown are results in the U.S. (a), southeastern U.S. (SEUS; b), Europe (c), eastern China (d), Beijing–Tianjin–Hebei (BTH; e), Jiangsu–Anhui–Shandong–Henan (SWLY; f), Yangtze River Delta (YRD; g), and Pearl River Delta (PRD; h) regions for observations (black) and simulations based on the SW-HRESM (red), low-resolution model with adjusted ozone dry deposition velocity of LE20_Wet (CESM-LR; blue), and LE20 ozone dry deposition scheme (CESM-LE20; orange). All observations and model simulations were combined to 1° prior to the analysis to exclude any influence solely caused by the grid spacing. The results of the student *t*-test demonstrate that the biases in SW-HRESM are significantly smaller, with all improvements being statistically significant ($p < 0.05$).

where the lower resolution grids may have captured some additional emissions from adjacent high-emission regions.

Some distinctive features emerge from the comparison. For all regions of interest, the low-resolution base simulations gave substantial overestimations, ranging from 6.0 to 16.2 ppbv, comparable to those reported previously (Emmons et al., 2020; Lamarque et al., 2012), although emissions in these studies may differ from that in this study. By adjusting the ozone dry deposition scheme to LE20_Wet, the simulated bias in the CESM-LR ranged from 4.7 to 10.8 ppbv, with a mean bias reduction of 19% (2.0 ppbv). By increasing the horizontal spatial resolution (SW-HRESM), the bias was further reduced by 43% (3.3 ppbv). Note that the mean bias in BTH is rather small, which does not mean SW-HRESM is perfect in simulating ozone concentrations. Instead, this reflects a five-summer mean simulated results without nudging, indicating the improvement of ozone simulations on the mean scale. One exception was found over Europe where the overestimation slightly increases in the SW-HRESM, which is consistent with a previous study (Fenech et al., 2018). A diagnostic analysis based on temperature showed that the SW-HRESM improved 2-m air temperature distribution, particularly on the high temperature flank over the right tail of temperature distributions, for most regions, except in Europe where there was a higher positive temperature bias compared to CESM-LR. This should be further investigated in future studies; for example, by conducting decadal simulations for assessment and applying a nudging technique to constrain the meteorology with observations. Another important feature is that the low-resolution model tends to underestimate the ozone peak, but overestimates low ozone values, whereas the SW-HRESM demonstrates enhanced capability for delineating both high and low peak ozone concentrations. By using another observational data set of TOAR, simulated results from SW-HRESM and CESM-LR at both urban (Figure S9 in Supporting Information S1), suburban and rural sites (Figure S10 in Supporting Information S1) show comparable conclusions to the discussions abovementioned.

Considering the new interim target 1 ozone standard of $160 \mu\text{g m}^{-3}$ (~ 80 ppbv) and target 2 ozone standard of $120 \mu\text{g m}^{-3}$ (~ 60 ppbv) released in the 2021 global air quality guidelines of the World Health Organization, as well as the standard of 70 ppbv set by the U.S. Environmental Protection Agency on 1 October 2015, we evaluated how the models behaved in terms of exceedance of these standards over metropolitan areas of China (e.g., BTH, SWLY, YRD, and PRD). As shown in Figure 5, the high-resolution model behaves much better in simulating the ozone exceedance days compared with the low-resolution simulations. Specifically, for the low-resolution ESM, the mean biases averaged over the ozone exceedance to the three standards of 60, 70, and 80 ppbv were 20%, 54%, 32%, and -58% over BTH, SWLY, YRD, and PRD, respectively, and the biases were reduced to 1%, 26%, -14% , and -26% , respectively, in the high-resolution simulations. Note that the very small bias in the SW-HRESM over BTH was partly caused by a positive bias in simulating the ozone exceedance at 60 and 70 ppbv, and a negative bias at 80 ppbv; however, none of the absolute biases were $>10\%$ for any of these standards. A negative bias indicates that there is room to improve the high-resolution model to simulate high ozone concentrations, such as those during episodic events.

3.3. Reasons for Ozone Improvement in High-Resolution Simulations

To elucidate the potential mechanisms behind the reduced ozone overestimation in high-resolution simulations, we first examined the diurnal cycles of ozone concentrations in observations and model simulations across different regions (Figure 6). This analysis revealed contrasting features between eastern China and the U.S. and Europe, which likely result from differences in observation site locations. In eastern China, most observation sites are located in urban areas, whereas in the U.S. and Europe, the majority of observations are taken in rural or suburban areas. Specifically, in the U.S., in the daytime, defined as 8:00 to 18:00 local standard time, the ozone difference between high- and low-resolution simulations was 2.8 ppbv, whereas at nighttime, defined as the hours outside of daytime, the ozone difference (1.3 ppbv) was less than half of that in the daytime. In eastern China, the ozone differences between high- and low-resolution simulations were comparably large in both the daytime (3.0 ppbv) and nighttime (3.0 ppbv). Over metropolitan areas (BTH), grid spacing could play a particularly important role in nighttime ozone simulations. For example, the daytime ozone difference (5.8 ppbv) between high- and low-resolution simulations was only two-thirds of that in the nighttime (8.8 ppbv). Moreover, for the PRD area, where summer is not the ozone season owing to high rainfall, heavy cloud cover and insufficient downward surface solar radiation (Kou et al., 2023), the differences in grid spacings affected the nighttime ozone difference (7.3 ppbv) by more than twice as much as that in the daytime (3.4 ppbv).

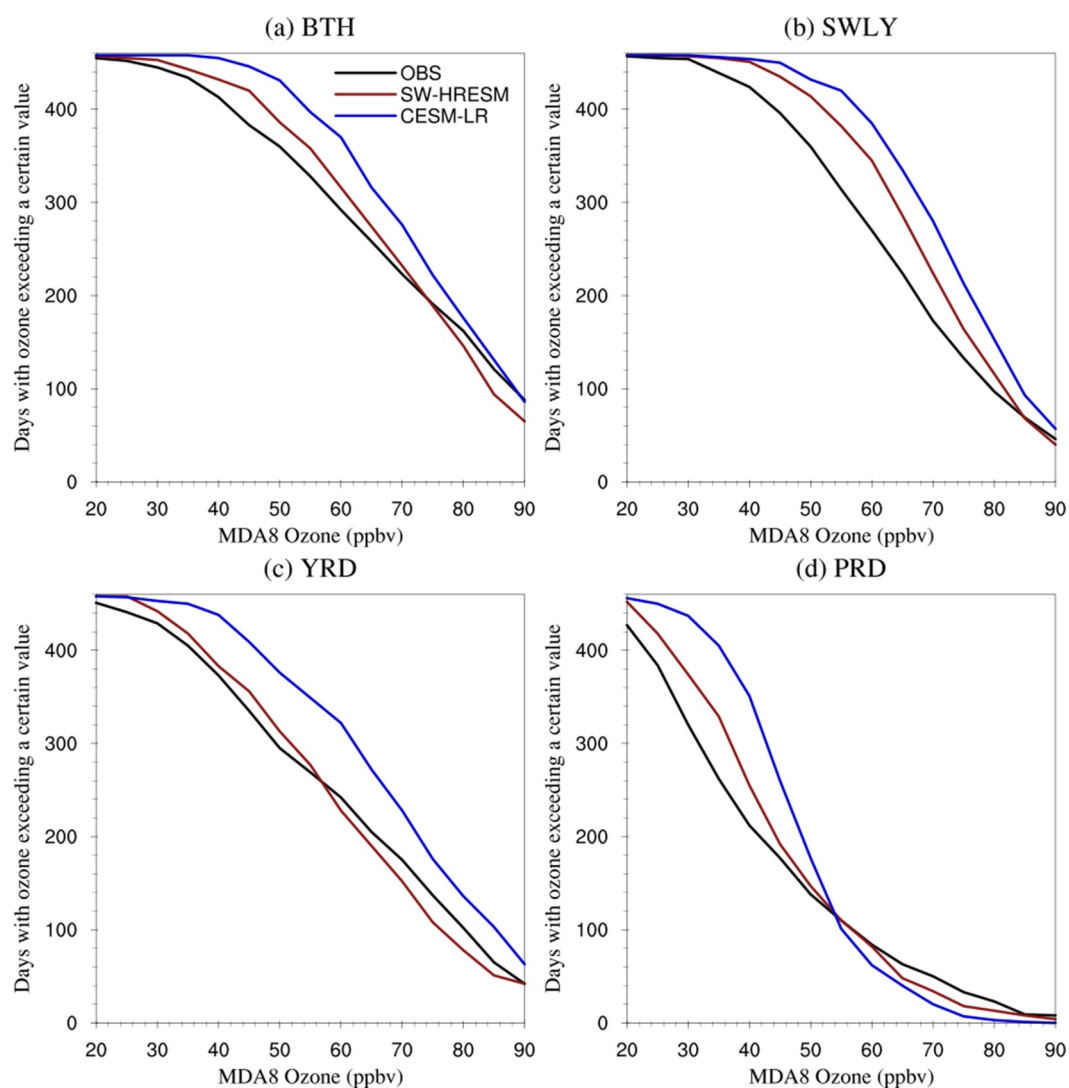


Figure 5. Days with ozone exceeding a certain value at x -axis. Shown are results during the summers of 2015–2019 in Beijing–Tianjin–Hebei (BTH; a), Jiangsu–Anhui–Shandong–Henan (SWLY; b), Yangtze River Delta (YRD; c), and Pearl River Delta (PRD; d) regions. The values on the x -axis start from 20 ppbv because there are few days with a mean MDA8 ozone <20 ppbv. Regional mean MDA8 ozone was applied prior to the calculation, and the same grids between observation and simulations were used in the comparison.

The phenomenon discussed above is likely associated with a shift in VOC-limited or NO_x -limited chemical regime. In the daytime, when photochemistry is strong, the mix of urban and rural areas in a coarse grid likely shifts the ozone regimes. For example, during the daytime, mixing of air at coarse grid scales may bring extra VOC emissions to NO_x -rich urban areas or NO_x emissions to rural areas (because rural areas typically have abundant VOC emissions and urban areas have abundant NO_x emissions), facilitating ozone formation and leading to ozone overestimation, which is the case for both the U.S. and eastern China. During the nighttime, NO titration over urban locations, which is frequently observed in eastern China, is weakened at a coarse resolution grid where NO is partly distributed to rural areas, leading to an ozone boost in urban areas. However, over rural areas, the addition of NO_x from urban areas does not play a large role because there are, in general, abundant VOC emissions but ozone is limited by weak photochemistry during the nighttime.

Two cities were selected to delve further into the mechanism of the way in which grid spacing may affect simulated daytime ozone. Los Angeles (34.5°N, 117.5°W) is a megacity that has faced ozone pollution for decades; the megacity of Shanghai (31.5°N, 121.5°E), having a comparable latitude to Los Angeles, was also selected. In Figure 7, we display the ozone concentrations in the two grids in which these cities are located from

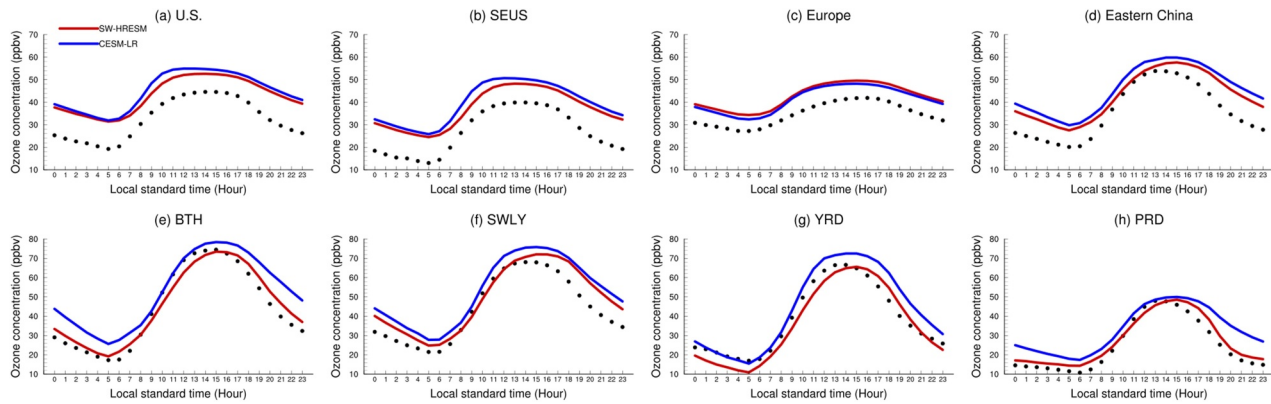


Figure 6. Diurnal cycles (local standard time) of ozone concentrations during the summers of 2015–2019. Regional mean ozone is shown for each region (a–h) by pairing the grids where observations exist. Observations are shown by the black dots and the CESM-LR and SW-HRESM simulations are shown by the blue and red curves, respectively. Note: SEUS = Southeastern U.S.; BTH = Beijing–Tianjin–Hebei; SWLY = Jiangsu–Anhui–Shandong–Henan; YRD = Yangtze River Delta; and PRD = Pearl River Delta.

the low-resolution model (CESM-LR; magenta dots), and the ozone concentrations in the corresponding 16 grids in the high-resolution model (SR-HRESM; red dots), as well as the observed ozone (black dots) in grids where data are available.

To delineate a VOC-limited or NO_x -limited regime, we selected the ratio of HCHO to NO_2 concentrations (HCHO/NO_2), which is a useful indicator to represent different ozone formation regimes (Martin et al., 2004; Schroeder et al., 2017, 2020). A HCHO/NO_2 value between 2.2 and 3.2 indicates a transition zone which is not too sensitive to either VOC or NO_x emissions; lower values tend to indicate a VOC-limited regime; and regions with higher values are likely NO_x -limited (Ren et al., 2022). Although the absolute threshold of HCHO/NO_2 separating VOC-limited and NO_x -limited regimes typically varies by location, the relative value should work well. Prior to interpretation of this ratio, we display the emission intensity of HCHO and NO_2 for the high- ($0.25^\circ \times 0.25^\circ$) and low-resolution ($1.0^\circ \times 1.0^\circ$) grids, over a $3^\circ \times 3^\circ$ square box centered by Los Angeles and Shanghai (Figures S11 and S12 in Supporting Information S1). Although the overall emission intensity is quite comparable between high- and low-resolution (in general within 10%) emissions over either Los Angeles or Shanghai, the spatial pattern could be quite different. The high-resolution emissions reveal much stronger spatial gradient which are largely missed in the low-resolution emissions.

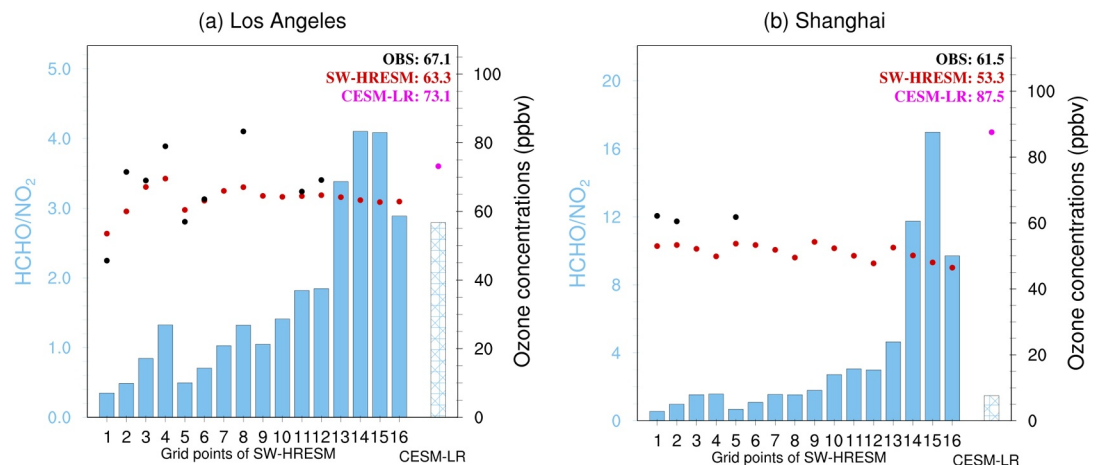


Figure 7. Mechanism governing daytime ozone differences between high- and low-resolution simulations. Shown are results from (a) Los Angeles and (b) Shanghai. The solid blue histograms show the ratios of HCHO to NO_2 , corresponding to the left-hand y-axis. The blue hatched histograms are from the CESM-LR, while the first 16 groups (histograms and dots) are data from the corresponding 16 grids in the high-resolution simulations. The dots represent the ozone concentrations from observations (black), SW-HRESM (red), and CESM-LR (magenta), and correspond to the right-hand y-axis.

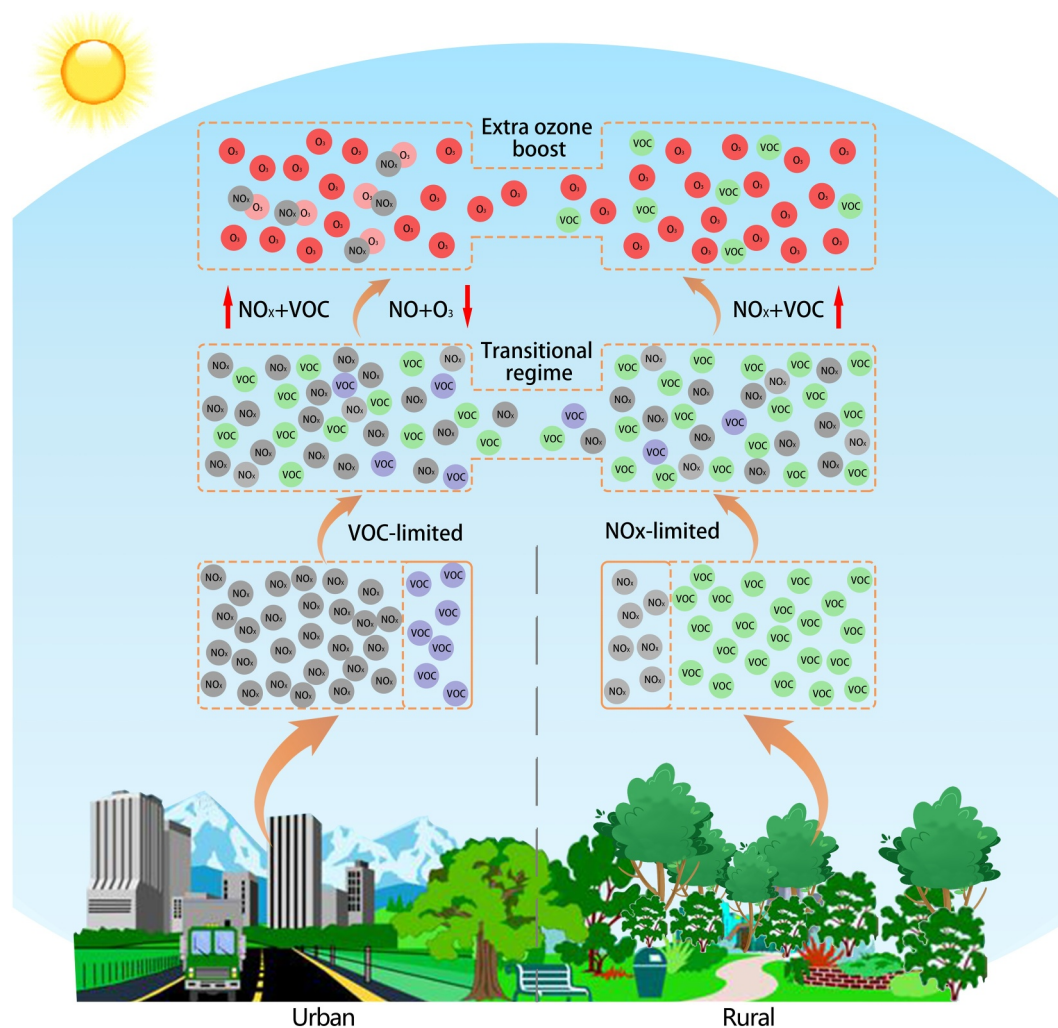


Figure 8. Schematic diagram of ozone simulations in urban and rural areas. In regions where urban and rural areas are adjacent to each other, urban areas generally tend to be VOC-limited and rural areas are NO_x-limited. Coarse grid spacings, such as 1° or larger, mix the urban and rural emission sources, resulting in urban NO_x emissions and rural VOC emissions being redistributed and mixed, forming a new transition zone that facilitates ozone formation in both areas during the daytime. During the nighttime, the assignment of urban NO_x emissions to rural areas may weaken urban NO titration, leading to ozone concentration increases.

In both Los Angeles and Shanghai, among the 16 grids, there is a mixture of VOC-limited and NO_x-limited regimes based on the HCHO/NO₂ ratio (solid blue histograms in Figure 7). However, after mixing these 16 grid boxes into a single grid box in the low-resolution model, heterogeneities in the ozone regimes result in a transitional regime in which VOC and NO_x emissions can more efficiently mix and react to form ozone, generally enhancing the ozone production efficiency and leading to an increase in ozone concentrations. This mechanism is depicted in the schematic diagram in Figure 8, which is well supported by the theoretical diagram shown in Figure 10 of Sillman et al. (1990a).

4. Discussion and Conclusions

In this study, a high-resolution Earth system model (SW-HRESM) was optimized computationally and physically to effectively simulate ozone concentrations. Targeting the long-standing issue of ozone overestimation in low-resolution Earth system models, by using one model of CESM, we first identified the ozone dry deposition velocity as a key variable contributing to this ozone bias. After adjusting the representation of stomatal conductance and leaf cuticle conductance, we achieved substantial model improvement by increasing the ozone

dry deposition velocity, which reduced the ozone overestimation to a certain extent. Given the lack of widespread observations of ozone dry deposition velocity, additional observational evidence in the future would greatly benefit model development and advance understanding of the role of ozone deposition.

Previous studies evaluating global simulated ozone have primarily focused on regions such as the U.S. and Europe owing to the availability of observational data, while regions with more severe ozone problems, such as eastern China, have received much less attention. We evaluated high-resolution ESM simulations, which greatly reduced the ozone biases present at low-resolution with the same model when compared to the observational data during 2015–2019. Furthermore, we determined that the mechanism behind bias reduction in these simulations (compared with the low-resolution counterpart) is associated with a shift in chemical regime, and that the biases show distinct diurnal differences between urban and rural areas. In rural areas, the effect of increased grid spacing has greatest effect during the daytime; for example, in a coarse resolution grid, extra NO_x emissions are distributed to rural areas, facilitating an ozone boost in these areas, leading to a large ozone overestimation. Over urban areas, the daytime mechanism is comparable to that in rural areas because there are extra VOC emissions coming from rural areas, thus enhancing ozone concentration. In contrast, during the nighttime, NO_x emissions assigned to rural areas in a coarse grid weaken NO titration over urban areas, and so there is reduced ozone removal during the nighttime over urban areas.

In this study, we examine the issue of ozone overestimation based on a high-resolution Earth system model. Considering that biases in historical simulations may alter the signal of future ozone changes under a warming climate, this newly optimized high-resolution Earth system model is expected to be very useful in enhancing understanding of ozone changes in the future and the associated impacts on human health and crops, which are vital issues that urgently require further investigation.

This study is subject to some limitations. Firstly, this study applies one high-resolution model, to demonstrate the usefulness of applying the finer resolution grid spacings in better resolving ozone chemistry regime, and more studies are called for in particular at the high-resolution scales to further warrant the robustness of the finding. Secondly, the horizontal resolution in this study is at 25 km, which not necessarily can fully resolve urban and rural areas, and an even higher horizontal resolution might be needed to better capture small-scale ozone dynamics and associated physical processes, such as deep convection (Marotzke, 2023). Thirdly, the assessment on surface ozone in this study is based on simulations without nudging, and changes in meteorology may yield different results. For instance, a study based on CESM simulations with regional refinement (as high as 7 km over Korea) indicates an overall improvement of high-resolution but not always (Jo et al., 2023). While we believe our overall findings of the contrasts between the high and low-resolution models should hold, how the high- and low-resolution models behave on the daily basis is of great interest to examine in future. Fourthly, recent studies based on regional models stress that biogenic emissions, important precursors of ozone, from urban greenspaces are often neglected, which can lead to underestimation of ozone formation during episodic events (Gao et al., 2022a; Ma et al., 2022). Although mean ozone concentration is overestimated in Earth system models, how they behave in episodic events remains an important issue to examine. And the missing of urban greenspaces is the fact in both high- and low-resolution models used in this study, and likely in many other models, which requires an urgent need to resolve upon ultrafine resolution land cover data, for example, at 10-m (Gbodjo et al., 2020; Xu et al., 2022). Lastly, the exchange between the stratosphere and troposphere can influence surface ozone concentrations, and the impact of the high-resolution modeling on STE still requires further investigation. Therefore, high-resolution Earth system model simulations on air quality remain to be great challenges by resolving all these issues and those not mentioned here, and community efforts might speed up the progress and eventually enhance the confidence of future air quality projections, as well as the interactions between climate and air quality.

Acknowledgments

This work was supported by the National Natural Science Foundation of China (42122039, 42375189) and the Science and Technology Innovation Project of Laoshan Laboratory (LSKJ202202200, LSKJ202202201). LRL were supported by Office of Science, U.S. Department of Energy (DOE) Biological and Environmental Research as part of the Regional and Global Model Analysis program area. Pacific Northwest National Laboratory is operated for DOE by Battelle Memorial Institute under contract DE-AC05-76RL01830. We acknowledge Lin Zhang and Han Han for their helpful discussions regarding the TOAR dataset, and thank the three anonymous reviewers for their helpful suggestions which have significantly helped improving the quality of the paper.

Data Availability Statement

The raw CESM model output data are available from the iHESP data portal (https://ihesp.github.io/archive/products/ihesp-products/data-release/DataRelease_Phase2.html).

References

- Ahmed, K., Shahid, S., Sachindra, D. A., Nawaz, N., & Chung, E.-S. (2019). Fidelity assessment of general circulation model simulated precipitation and temperature over Pakistan using a feature selection method. *Journal of Hydrology*, 573, 281–298. <https://doi.org/10.1016/j.jhydrol.2019.03.092>

- Bacmeister, J. T., Wehner, M. F., Neale, R. B., Gettelman, A., Hannay, C., Lauritzen, P. H., et al. (2014). Exploratory high-resolution climate simulations using the community atmosphere model (CAM). *Journal of Climate*, 27(9), 3073–3099. <https://doi.org/10.1175/JCLI-D-13-00387.1>
- Baldocchi, D. D., Hicks, B. B., & Camara, P. (1987). A canopy stomatal resistance model for gaseous deposition to vegetated surfaces. *Atmospheric Environment*, 21(1), 91–101. [https://doi.org/10.1016/0004-6981\(87\)90274-5](https://doi.org/10.1016/0004-6981(87)90274-5)
- Boyle, J., & Klein, S. A. (2010). Impact of horizontal resolution on climate model forecasts of tropical precipitation and diabatic heating for the TWP-ICE period. *Journal of Geophysical Research*, 115(D23). <https://doi.org/10.1029/2010JD014262>
- Caldwell, P. M., Mamejtanov, A., Tang, Q., Van Roekel, L. P., Golaz, J., Lin, W., et al. (2019). The DOE E3SM coupled model version 1: Description and results at high resolution. *Journal of Advances in Modeling Earth Systems*, 11(12), 4095–4146. <https://doi.org/10.1029/2019MS001870>
- Chang, P., Zhang, S., Danabasoglu, G., Yeager, S. G., Fu, H., Wang, H., et al. (2020). An unprecedented set of high-resolution earth system simulations for understanding multiscale interactions in climate variability and change. *Journal of Advances in Modeling Earth Systems*, 12, e2020MS002298. <https://doi.org/10.1029/2020MS002298>
- Chen, L., Gao, Y., Ma, M., Wang, L., Wang, Q., Guan, S., et al. (2023). Striking impacts of biomass burning on PM2.5 concentrations in Northeast China through the emission inventory improvement. *Environmental Pollution*, 318, 120835. <https://doi.org/10.1016/j.envpol.2022.120835>
- Clifton, O. E., Fiore, A. M., Massman, W. J., Baublitz, C. B., Coyle, M., Emberson, L., et al. (2020). Dry deposition of ozone over land: Processes, measurement, and modeling. *Reviews of Geophysics*, 58(1), e2019RG000670. <https://doi.org/10.1029/2019RG000670>
- Clifton, O. E., Paulot, F., Fiore, A. M., Horowitz, L. W., Correa, G., Baublitz, C. B., et al. (2020). Influence of dynamic ozone dry deposition on ozone pollution. *Journal of Geophysical Research: Atmospheres*, 125(8). <https://doi.org/10.1029/2020jd032398>
- Collatz, G. J., Ball, J. T., Grivet, C., & Berry, J. A. (1991). Physiological and environmental regulation of stomatal conductance, photosynthesis and transpiration: A model that includes a laminar boundary layer. *Agricultural and Forest Meteorology*, 54(2–4), 107–136. [https://doi.org/10.1016/0168-1923\(91\)90002-8](https://doi.org/10.1016/0168-1923(91)90002-8)
- Collatz, G. J., Ribas-Carbo, M., & Berry, J. A. (1992). Coupled photosynthesis-stomatal conductance model for leaves of C4 plants. *Functional Plant Biology*, 19(5), 519–538. <https://doi.org/10.1071/PP9920519>
- Collins, W. J., Lamarque, J. F., Schulz, M., Boucher, O., Eyring, V., Hegglin, M. I., et al. (2017). AerChemMIP: Quantifying the effects of chemistry and aerosols in CMIP6. *Geoscientific Model Development*, 10(2), 585–607. <https://doi.org/10.5194/gmd-10-585-2017>
- Dentener, F., Kinne, S., Bond, T., Boucher, O., Cofala, J., Generoso, S., et al. (2006). Emissions of primary aerosol and precursor gases in the years 2000 and 1750 prescribed data-sets for AeroCom. *Atmospheric Chemistry and Physics*, 6(12), 4321–4344. <https://doi.org/10.5194/acp-6-4321-2006>
- El-Madany, T. S., Niklasch, K., & Klemm, O. (2017). Stomatal and non-stomatal turbulent deposition flux of ozone to a managed peatland. *Atmosphere*, 8(9), 175. <https://doi.org/10.3390/atmos8090175>
- Emmons, L. K., Schwantes, R. H., Orlando, J. J., Tyndall, G., Kinnison, D., Lamarque, J., et al. (2020). The chemistry mechanism in the community earth system model version 2 (CESM2). *Journal of Advances in Modeling Earth Systems*, 12(4), e2019MS001882. <https://doi.org/10.1029/2019MS001882>
- Emmons, L. K., Walters, S., Hess, P. G., Lamarque, J. F., Pfister, G. G., Fillmore, D., et al. (2010). Description and evaluation of the model for ozone and related chemical Tracers, version 4 (MOZART-4). *Geoscientific Model Development*, 3(1), 43–67. <https://doi.org/10.5194/gmd-3-43-2010>
- Fares, S., Savi, F., Muller, J., Matteucci, G., & Paoletti, E. (2014). Simultaneous measurements of above and below canopy ozone fluxes help partitioning ozone deposition between its various sinks in a Mediterranean Oak Forest. *Agricultural and Forest Meteorology*, 198–199, 181–191. <https://doi.org/10.1016/j.agrformet.2014.08.014>
- Fenech, S., Doherty, R. M., Heaviside, C., Vardoulakis, S., Macintyre, H. L., & O'Connor, F. M. (2018). The influence of model spatial resolution on simulated ozone and fine particulate matter for Europe: Implications for health impact assessments. *Atmospheric Chemistry and Physics*, 18(8), 5765–5784. <https://doi.org/10.5194/acp-18-5765-2018>
- Finkelstein, P. L., Ellestad, T. G., Clarke, J. F., Meyers, T. P., Schwede, D. B., Hebert, E. O., & Neal, J. A. (2000). Ozone and sulfur dioxide dry deposition to forests: Observations and model evaluation. *Journal of Geophysical Research*, 105(D12), 15365–15377. <https://doi.org/10.1029/2000JD900185>
- Fiore, A. M., Naik, V., & Leibensperger, E. M. (2015). Air quality and climate connections. *Journal of the Air & Waste Management Association*, 65(6), 645–685. <https://doi.org/10.1080/109662247.2015.1040526>
- Fleming, Z. L., Doherty, R. M., von Schneidmesser, E., Malley, C. S., Cooper, O. R., Pinto, J. P., et al. (2018). Tropospheric Ozone Assessment Report: Present-day ozone distribution and trends relevant to human health. *Elementa-Sci. Anthropol.*, 6. <https://doi.org/10.1525/elementa.273>
- Forkel, R., & Knoche, R. (2007). Nested regional climate–chemistry simulations for central Europe. *Comptes Rendus Geoscience*, 339(11–12), 734–746. <https://doi.org/10.1016/j.crte.2007.09.018>
- Fowler, D., Flechard, C., Cape, J. N., Storeton-West, R. L., & Coyle, M. (2001). Measurements of ozone deposition to vegetation quantifying the flux, the stomatal and non-stomatal components. *Water, Air, and Soil Pollution*, 130(1/4), 63–74. <https://doi.org/10.1023/A:1012243317471>
- Fowler, D., Pilegaard, K., Sutton, M., Ambus, P., Raivonen, M., Duyzer, J., et al. (2009). Atmospheric composition change: Ecosystems–Atmosphere interactions. *Atmospheric Environment*, 43(33), 5193–5267. <https://doi.org/10.1016/j.atmosenv.2009.07.068>
- Fu, T. M., & Tian, H. (2019). Climate change penalty to ozone air quality: Review of current understandings and knowledge gaps. *Current Pollution Reports*, 5(3), 159–171. <https://doi.org/10.1007/s40726-019-00115-6>
- Gao, W., & Wesely, M. L. (1995). Modeling gaseous dry deposition over regional scales with satellite observations—I. Model development. *Atmospheric Environment*, 29(6), 727–737. [https://doi.org/10.1016/1352-2310\(94\)00284-R](https://doi.org/10.1016/1352-2310(94)00284-R)
- Gao, Y., Guo, X., Lu, J., Woolings, T., Chen, D., Guo, X., et al. (2025). Enhanced simulation of atmospheric blocking in a high-resolution earth system model: Projected changes and implications for extreme weather events. *J. Geophys. Res.-Atmos.*, 130(3), e2024JD042045. <https://doi.org/10.1029/2024JD042045>
- Gao, Y., Ma, M., Yan, F., Su, H., Wang, S., Liao, H., et al. (2022a). Impacts of biogenic emissions from urban landscapes on summer ozone and secondary organic aerosol formation in megacities. *Science of the Total Environment*, 814, 152654. <https://doi.org/10.1016/j.scitotenv.2021.152654>
- Gao, Y., Wu, Y., Guo, X., Kou, W., Zhang, S., Leung, L. R., et al. (2023). More frequent and persistent heatwaves due to increased temperature skewness projected by a high-resolution earth system model. *Geophysical Research Letters*, 50(18), e2023GL105840. <https://doi.org/10.1029/2023GL105840>
- Gao, Y., Zhang, J., Yan, F., Leung, L. R., Luo, K., Zhang, Y., & Bell, M. L. (2020). Nonlinear effect of compound extreme weather events on ozone formation over the United States. *Weather and Climate Extremes*, 30, 100285. <https://doi.org/10.1016/j.wace.2020.100285>

- Gao, Y., Zhang, L., Huang, A., Kou, W., Bo, X., Cai, B., & Qu, J. (2022b). Unveiling the spatial and sectoral characteristics of a high-resolution emission inventory of CO₂ and air pollutants in China. *Science of the Total Environment*, *847*, 157623. <https://doi.org/10.1016/j.scitotenv.2022.157623>
- Gbodjo, Y. J. E., Ienco, D., & Leroux, L. (2020). Toward spatio-spectral analysis of Sentinel-2 time series data for land cover mapping. *IEEE Geoscience and Remote Sensing Letters*, *17*, 307–311. <https://doi.org/10.1109/LGRS.2019.2917788>
- Golaz, J.-C., Caldwell, P. M., Van Roekel, L. P., Petersen, M. R., Tang, Q., Wolfe, J. D., et al. (2019). The DOE E3SM coupled model version 1: Overview and evaluation at standard resolution. *Journal of Advances in Modeling Earth Systems*, *11*(7), 2089–2129. <https://doi.org/10.1029/2018MS001603>
- Granier, C., Darras, S., van Der Gon, H. D., Doubalova, J., Elguindi, N., Galle, B., et al. (2019). The copernicus atmosphere monitoring service global and regional emissions (April 2019 version). Copernicus Atmosphere Monitoring Service (CAMS) report. <https://doi.org/10.24380/d0bn-kx16>
- Guan, S., Wong, D. C., Gao, Y., Zhang, T., & Pouliot, G. (2020). Impact of wildfire on particulate matter in the southeastern United States in November 2016. *Science of the Total Environment*, *724*, 138354. <https://doi.org/10.1016/j.scitotenv.2020.138354>
- Guenther, A. B., Jiang, X., Heald, C. L., Sakulyanontvittaya, T., Duhl, T., Emmons, L. K., & Wang, X. (2012). The model of emissions of gases and aerosols from nature version 2.1 (MEGAN2.1): An extended and updated framework for modeling biogenic emissions. *Geoscientific Model Development*, *5*(6), 1471–1492. <https://doi.org/10.5194/gmd-5-1471-2012>
- Guo, X., Gao, Y., Zhang, S., Cai, W., Leung, L. R., Lu, J., et al. (2024). More high-impact atmospheric river-induced extreme precipitation events under warming in a high-resolution model. *One Earth*, *7*(12), 2223–2234. <https://doi.org/10.1016/j.oneear.2024.11.009>
- Guo, X., Gao, Y., Zhang, S., Wu, L., Chang, P., Cai, W., et al. (2022). Threat by marine heatwaves to adaptive large marine ecosystems in an eddy-resolving model. *Nature Climate Change*, *12*(2), 179–186. <https://doi.org/10.1038/s41558-021-01266-5>
- Hardacre, C., Wild, O., & Emberson, L. (2015). An evaluation of ozone dry deposition in global scale chemistry climate models. *Atmospheric Chemistry and Physics*, *15*(11), 6419–6436. <https://doi.org/10.5194/acp-15-6419-2015>
- Hoesly, R. M., Smith, S. J., Feng, L., Klimont, Z., Janssens-Maenhout, G., Pitkanen, T., et al. (2018). Historical (1750–2014) anthropogenic emissions of reactive gases and aerosols from the Community Emissions Data System (CEDS). *Geoscientific Model Development*, *11*(1), 369–408. <https://doi.org/10.5194/gmd-11-369-2018>
- Hsu, J., & Prather, M. J. (2009). Stratospheric variability and tropospheric ozone. *Journal of Geophysical Research*, *114*(D6). <https://doi.org/10.1029/2008JD010942>
- Huang, Y., Dickinson, R. E., & Chameides, W. L. (2006). Impact of aerosol indirect effect on surface temperature over East Asia. *Proceedings of the National Academy of Sciences of the United States of America*, *103*(12), 4371–4376. <https://doi.org/10.1073/pnas.0504428103>
- Jacob, D. J., & Winner, D. A. (2009). Effect of climate change on air quality. *Atmospheric Environment*, *43*(1), 51–63. <https://doi.org/10.1016/j.atmosenv.2008.09.051>
- Jo, D. S., Emmons, L. K., Callaghan, P., Tilmes, S., Woo, J., Kim, Y., et al. (2023). Comparison of urban air quality simulations during the KORUS-AQ campaign with regionally refined versus global uniform grids in the multi-scale infrastructure for chemistry and aerosols (MUSICA) version 0. *Journal of Advances in Modeling Earth Systems*, *15*(7), e2022MS003458. <https://doi.org/10.1029/2022MS003458>
- Khodayari, A., Vitt, F., Phoenix, D., & Wuebbles, D. J. (2018). The impact of NO_x emissions from lightning on the production of aviation-induced ozone. *Atmospheric Environment*, *187*, 410–416. <https://doi.org/10.1016/j.atmosenv.2018.05.057>
- Kleinman, L. I. (2000). Ozone process insights from field experiments – Part II: Observation-based analysis for ozone production. *Atmospheric Environment*, *34*(12–14), 2023–2033. [https://doi.org/10.1016/S1352-2310\(99\)00457-4](https://doi.org/10.1016/S1352-2310(99)00457-4)
- Kou, W., Gao, Y., Tong, D., Guo, X., An, X., Liu, W., et al. (2025). Enhanced understanding of atmospheric blocking modulation on ozone dynamics within a high-resolution Earth system model. *EGU sphere*. <https://doi.org/10.5194/egusphere-2024-2500>
- Kou, W., Gao, Y., Zhang, S., Cai, W., Geng, G., Davis, S. J., et al. (2023). High downward surface solar radiation conducive to ozone pollution more frequent under global warming. *Scientific Bulletin*, *68*(4), 388–392. <https://doi.org/10.1016/j.scib.2023.01.022>
- Lamarque, J. F., Emmons, L. K., Hess, P. G., Kinnison, D. E., Tilmes, S., Vitt, F., et al. (2012). CAM-Chem: Description and evaluation of interactive atmospheric chemistry in the community earth system model. *Geoscientific Model Development*, *5*(2), 369–411. <https://doi.org/10.5194/gmd-5-369-2012>
- Lamarque, J. F., Shindell, D. T., Josse, B., Young, P. J., Cionni, I., Eyring, V., et al. (2013). The atmospheric chemistry and climate model intercomparison project (ACCMIP): Overview and description of models, simulations and climate diagnostics. *Geoscientific Model Development*, *6*(1), 179–206. <https://doi.org/10.5194/gmd-6-179-2013>
- Lambert, S. J., & Boer, G. J. (2001). CMIP1 evaluation and intercomparison of coupled climate models. *Climate Dynamics*, *17*(2–3), 83–106. <https://doi.org/10.1007/PL00013736>
- Lauwaet, D., Viaene, P., Brisson, E., van Lipzig, N., van Noije, T., Strunk, A., et al. (2014). The effect of climate change and emission scenarios on ozone concentrations over Belgium: A high-resolution model study for policy support. *Atmospheric Chemistry and Physics*, *14*(12), 5893–5904. <https://doi.org/10.5194/acp-14-5893-2014>
- Lelieveld, J., Evans, J. S., Fnais, M., Giannadaki, D., & Pozzer, A. (2015). The contribution of outdoor air pollution sources to premature mortality on a global scale. *Nature*, *525*(7569), 367–371. <https://doi.org/10.1038/nature15371>
- Li, J., Nagashima, T., Kong, L., Ge, B., Yamaji, K., Fu, J. S., et al. (2019). Model evaluation and intercomparison of surface-level ozone and relevant species in East Asia in the context of MICS-Asia phase III – Part 1: Overview. *Atmospheric Chemistry and Physics*, *19*(20), 12993–13015. <https://doi.org/10.5194/acp-19-12993-2019>
- Li, M., Liu, H., Geng, G., Hong, C., Liu, F., Song, Y., et al. (2017). Anthropogenic emission inventories in China: A review. *National Science Review*, *4*(6), 834–866. <https://doi.org/10.1093/nsr/nwx150>
- Li, Q., Gabay, M., Rubin, Y., Fredj, E., & Tas, E. (2018). Measurement-based investigation of ozone deposition to vegetation under the effects of coastal and photochemical air pollution in the Eastern Mediterranean. *Science of the Total Environment*, *645*, 1579–1597. <https://doi.org/10.1016/j.scitotenv.2018.07.037>
- Liao, H., Gao, Y., Chen, D., Dai, H., Du, N., Fang, L., et al. (2021). Assessment of air quality-climate interactions in IPCC AR6. *Trans. Atmospheric Science*, *44*, 658–666. <https://doi.org/10.13878/j.cnki.dqkxxb.20210823011>
- Liu, S. C., Trainer, M., Fehsenfeld, F. C., Parrish, D. D., Williams, E. J., Fahey, D. W., et al. (1987). Ozone production in the rural troposphere and the implications for regional and global ozone distributions. *Journal of Geophysical Research*, *92*(D4), 4191–4207. <https://doi.org/10.1029/JD092iD04p04191>
- Liu, X., Easter, R. C., Ghan, S. J., Zaveri, R., Rasch, P., Shi, X., et al. (2012). Toward a minimal representation of aerosols in climate models: Description and evaluation in the community atmosphere model CAM5. *Geoscientific Model Development*, *5*(3), 709–739. <https://doi.org/10.5194/gmd-5-709-2012>

- Ma, M., Gao, Y., Ding, A., Su, H., Liao, H., Wang, S., et al. (2022). Development and assessment of a high-resolution biogenic emission inventory from urban green spaces in China. *Environmental Science & Technology*, *56*(1), 175–184. <https://doi.org/10.1021/acs.est.1c06170>
- Madronich, S. (1993). The atmosphere and UV-B radiation at ground level. In A. R. Young, J. Moan, L. O. Björn, & W. Nultsch (Eds.), *Environmental UV photobiology* (pp. 1–39). Springer US.
- Markakis, K., Valari, M., Colette, A., Sanchez, O., Perrussel, O., Honore, C., et al. (2014). Air quality in the mid-21st century for the city of Paris under two climate scenarios; from the regional to local scale. *Atmospheric Chemistry and Physics*, *14*, 7323–7340. <https://doi.org/10.5194/acp-14-7323-2014>
- Markakis, K., Valari, M., Engardt, M., Lacressonniere, G., Vautard, R., & Andersson, C. (2016). Mid-21st century air quality at the urban scale under the influence of changed climate and emissions – Case studies for Paris and Stockholm. *Atmospheric Chemistry and Physics*, *16*(4), 1877–1894. <https://doi.org/10.5194/acp-16-1877-2016>
- Marotzke, J. (2023). From theory to RAPID AMOC observations: A personal voyage of discovery. *Philosophical Transactions of the Royal Society A*, *381*(2262), 20220192. <https://doi.org/10.1098/rsta.2022.0192>
- Martin, R. V., Fiore, A. M., & Van Donkelaar, A. (2004). Space-based diagnosis of surface ozone sensitivity to anthropogenic emissions. *Geophysical Research Letters*, *31*(6). <https://doi.org/10.1029/2004GL019416>
- Meehl, G. A., Yang, D., Arblaster, J. M., Bates, S. C., Rosenbloom, N., Neale, R., et al. (2019). Effects of model resolution, physics, and coupling on southern Hemisphere storm tracks in CESM1.3. *Geophysical Research Letters*, *46*(21), 12408–12416. <https://doi.org/10.1029/2019GL084057>
- Meyers, T. P., Finkelstein, P., Clarke, J., Ellestad, T. G., & Sims, P. F. (1998). A multilayer model for inferring dry deposition using standard meteorological measurements. *Journal of Geophysical Research*, *103*(D17), 22645–22661. <https://doi.org/10.1029/98JD01564>
- Mills, G., Pleijel, H., Malley, C. S., Sinha, B., Cooper, O. R., Schultz, M. G., et al. (2018). Tropospheric Ozone Assessment Report: Present-day tropospheric ozone distribution and trends relevant to vegetation. *Elementa-Sci. Anthropol.*, *6*. <https://doi.org/10.1525/elementa.302>
- Morgenstern, O., Giorgetta, M. A., Shibata, K., Eyring, V., Waugh, D. W., Shepherd, T. G., et al. (2010). Review of the formulation of present-generation stratospheric chemistry-climate models and associated external forcings. *Journal of Geophysical Research*, *115*(D3). <https://doi.org/10.1029/2009JD013728>
- Morgenstern, O., Hegglin, M. I., Rozanov, E., O'Connor, F. M., Abraham, N. L., Akiyoshi, H., et al. (2017). Review of the global models used within phase 1 of the chemistry–climate model initiative (CCMI). *Geoscientific Model Development*, *10*(2), 639–671. <https://doi.org/10.5194/gmd-10-639-2017>
- Padro, J. (1996). Summary of ozone dry deposition velocity measurements and model estimates over vineyard, cotton, grass and deciduous forest in summer. *Atmospheric Environment*, *30*(13), 2363–2369. [https://doi.org/10.1016/1352-2310\(95\)00352-5](https://doi.org/10.1016/1352-2310(95)00352-5)
- Prather, M. J., Zhu, X., Tang, Q., Hsu, J., & Neu, J. L. (2011). An atmospheric chemist in search of the tropopause. *Journal of Geophysical Research*, *116*(D4), D04306. <https://doi.org/10.1029/2010JD014939>
- Price, C., Penner, J., & Prather, M. (1997). NOx from lightning: 1. Global distribution based on lightning physics. *Journal of Geophysical Research*, *102*(D5), 5929–5941. <https://doi.org/10.1029/96JD03504>
- Price, C., & Rind, D. (1992). A simple lightning parameterization for calculating global lightning distributions. *Journal of Geophysical Research*, *97*(D9), 9919–9933. <https://doi.org/10.1029/92JD00719>
- Quaas, J., Ming, Y., Menon, S., Takemura, T., Wang, M., Penner, J. E., et al. (2009). Aerosol indirect effects – General circulation model intercomparison and evaluation with satellite data. *Atmospheric Chemistry and Physics*, *9*(22), 8697–8717. <https://doi.org/10.5194/acp-9-8697-2009>
- Ramanathan, V., Crutzen, P. J., Kiehl, J. T., & Rosenfeld, D. (2001). Aerosols, climate, and the hydrological cycle. *Science*, *294*(5549), 2119–2124. <https://doi.org/10.1126/science.1064034>
- Ren, J., Guo, F., & Xie, S. (2022). Diagnosing ozone–NOx–VOC sensitivity and revealing causes of ozone increases in China based on 2013–2021 satellite retrievals. *Atmospheric Chemistry and Physics*, *22*, 15035–15047. <https://doi.org/10.5194/acp-22-15035-2022>
- Schroeder, J. R., Crawford, J. H., Ahn, J. Y., Chang, L., Fried, A., Walega, J., et al. (2020). Observation-based modeling of ozone chemistry in the seoul metropolitan area during the Korea–United States air quality study (KORUS-AQ). *Elementa: Science of the Anthropocene*, *8*. <https://doi.org/10.1525/elementa.400>
- Schroeder, J. R., Crawford, J. H., Fried, A., Walega, J., Weinheimer, A., Wisthaler, A., et al. (2017). New insights into the column CH₂O/NO₂ ratio as an indicator of near-surface ozone sensitivity. *Journal of Geophysical Research: Atmospheres*, *122*(16), 8885–8907. <https://doi.org/10.1002/2017JD026781>
- Schwantes, R. H., Lacey, F. G., Tilmes, S., Emmons, L. K., Lauritzen, P. H., Walters, S., et al. (2022). Evaluating the impact of chemical complexity and horizontal resolution on tropospheric ozone over the conterminous US with a global variable resolution chemistry model. *Journal of Advances in Modeling Earth Systems*, *14*(6), e2021MS002889. <https://doi.org/10.1029/2021MS002889>
- Schwede, D., Zhang, L., Vet, R., & Lear, G. (2011). An intercomparison of the deposition models used in the CASTNET and CAPMoN networks. *Atmospheric Environment*, *45*(6), 1337–1346. <https://doi.org/10.1016/j.atmosenv.2010.11.050>
- Sellers, P. J., Tucker, C. J., Collatz, G. J., Los, S. O., Justice, C. O., Dazlich, D. A., & Randall, D. A. (1996). A revised land surface parameterization (SiB2) for atmospheric GCMS. Part II: The generation of global fields of terrestrial biophysical parameters from satellite data. *Journal of Climate*, *9*(4), 706–737. [https://doi.org/10.1175/1520-0442\(1996\)009<0706:Arslpf>2.0.Co;2](https://doi.org/10.1175/1520-0442(1996)009<0706:Arslpf>2.0.Co;2)
- Shao, M., Yang, J. B., Wang, J. M., Chen, P. L., Liu, B. S., & Dai, Q. L. (2022). Co-occurrence of surface O₃, PM_{2.5} pollution, and tropical cyclones in China. *Journal of Geophysical Research: Atmospheres*, *127*(14). <https://doi.org/10.1029/2021JD036310>
- Sillman, S., Logan, J. A., & Wofsy, S. C. (1990a). A regional scale model for ozone in the United States with subgrid representation of urban and power plant plumes. *Journal of Geophysical Research*, *95*(D5), 5731–5748. <https://doi.org/10.1029/JD095iD05p05731>
- Sillman, S., Logan, J. A., & Wofsy, S. C. (1990b). The sensitivity of ozone to nitrogen oxides and hydrocarbons in regional ozone episodes. *Journal of Geophysical Research*, *95*(D2), 1837–1851. <https://doi.org/10.1029/JD095iD02p01837>
- Stevens, B., Adami, S., Ali, T., Anzt, H., Aslan, Z., Attinger, S., et al. (2023). Earth virtualization engines (EVE). *Earth System Science Data Discussions*, *2023*, 1–14. <https://doi.org/10.5194/essd-2023-376>
- Szopa, S., Naik, V., Adhikary, B., Artaxo, P., Bernsten, T., Collins, W. D., et al. (2021). Short-lived climate forcers. In *Climate change 2021: The physical science basis. Contribution of working group I to the sixth assessment report of the intergovernmental Panel on climate change* (pp. 817–922). Cambridge University Press. <https://doi.org/10.1017/9781009157896.008>
- Tang, W., Emmons, L. K., Buchholz, R. R., Wiedinmyer, C., Schwantes, R. H., He, C., et al. (2022). Effects of fire diurnal variation and plume rise on U.S. Air quality during FIREX-AQ and WE-CAN based on the multi-scale infrastructure for chemistry and aerosols (MUSICAv0). *Journal of Geophysical Research: Atmospheres*, *127*(16), e2022JD036650. <https://doi.org/10.1029/2022JD036650>
- Terai, C. R., Caldwell, P. M., Klein, S. A., Tang, Q., & Branstetter, M. L. (2018). The atmospheric hydrologic cycle in the ACME v0.3 model. *Climate Dynamics*, *50*(9–10), 3251–3279. <https://doi.org/10.1007/s00382-017-3803-x>

- Thorsen, T. J., Ferrare, R. A., Kato, S., & Winker, D. M. (2020). Aerosol direct radiative effect sensitivity analysis. *Journal of Climate*, *33*(14), 6119–6139. <https://doi.org/10.1175/JCLI-D-19-0669.1>
- Turnock, S. T., Allen, R. J., Andrews, M., Bauer, S. E., Deushi, M., Emmons, L., et al. (2020). Historical and future changes in air pollutants from CMIP6 models. *Atmospheric Chemistry and Physics*, *20*(23), 14547–14579. <https://doi.org/10.5194/acp-20-14547-2020>
- Val Martin, M., Heald, C. L., & Arnold, S. R. (2014). Coupling dry deposition to vegetation phenology in the Community Earth System Model: Implications for the simulation of surface O₃. *Geophysical Research Letters*, *41*(8), 2988–2996. <https://doi.org/10.1002/2014GL059651>
- von Schneidemesser, E., Monks, P. S., Allan, J. D., Bruhwiler, L., Forster, P., Fowler, D., et al. (2015). Chemistry and the linkages between air quality and climate change. *Chemistry Review*, *115*(10), 3856–3897. <https://doi.org/10.1021/acs.chemrev.5b00089>
- Wang, T., Xue, L., Brimblecombe, P., Lam, Y. F., Li, L., & Zhang, L. (2017). Ozone pollution in China: A review of concentrations, meteorological influences, chemical precursors, and effects. *Science of the Total Environment*, *575*, 1582–1596. <https://doi.org/10.1016/j.scitotenv.2016.10.081>
- Wesely, M. L. (1989). Parameterization of surface resistances to gaseous dry deposition in regional-scale numerical models. *Atmospheric Environment*, *23*(6), 1293–1304. [https://doi.org/10.1016/0004-6981\(89\)90153-4](https://doi.org/10.1016/0004-6981(89)90153-4)
- Wesely, M. L., & Hicks, B. B. (2000). A review of the current status of knowledge on dry deposition. *Atmospheric Environment*, *34*, 2261–2282. [https://doi.org/10.1016/S1352-2310\(99\)00467-7](https://doi.org/10.1016/S1352-2310(99)00467-7)
- Wiedinmyer, C., Akagi, S. K., Yokelson, R. J., Emmons, L. K., Al-Saadi, J. A., Orlando, J. J., & Soja, A. J. (2011). The fire INventory from NCAR (FINN): A high resolution global model to estimate the emissions from open burning. *Geoscientific Model Development*, *4*(3), 625–641. <https://doi.org/10.5194/gmd-4-625-2011>
- Wiedinmyer, C., & Emmons, L. (2022). Fire inventory from NCAR version 2 fire emission. *Research Data Archive at the National Center for Atmospheric Research, Computational and Information Systems Laboratory*. <https://doi.org/10.5065/XNPA-AF09>
- Wiedinmyer, C., Kimura, Y., McDonald-Buller, E. C., Emmons, L. K., Buchholz, R. R., Tang, W., et al. (2023). The fire inventory from NCAR version 2.5: An updated global fire emissions model for climate and chemistry applications. *Geoscientific Model Development*, *16*(13), 3873–3891. <https://doi.org/10.5194/gmd-16-3873-2023>
- Wild, O., & Prather, M. J. (2006). Global tropospheric ozone modeling: Quantifying errors due to grid resolution. *Journal of Geophysical Research*, *111*(D11). <https://doi.org/10.1029/2005JD006605>
- Williamson, D. L. (2013). The effect of time steps and time-scales on parametrization suites. *Quarterly Journal of the Royal Meteorological Society*, *139*(671), 548–560. <https://doi.org/10.1002/qj.1992>
- Wu, Z., Schwede, D. B., Vet, R., Walker, J. T., Shaw, M., Staebler, R., & Zhang, L. (2018). Evaluation and intercomparison of five north American dry deposition algorithms at a mixed forest site. *Journal of Advances in Modeling Earth Systems*, *10*(7), 1571–1586. <https://doi.org/10.1029/2017ms001231>
- Xie, S., Lin, W., Rasch, P. J., Ma, P., Neale, R., Larson, V. E., et al. (2018). Understanding cloud and convective characteristics in version 1 of the E3SM atmosphere model. *Journal of Advances in Modeling Earth Systems*, *10*, 2618–2644. <https://doi.org/10.1029/2018MS001350>
- Xu, F., Heremans, S., & Somers, B. (2022). Urban land cover mapping with Sentinel-2: A spectro-spatio-temporal analysis. *Urban Informatics*, *1*, 8. <https://doi.org/10.1007/s44212-022-00008-y>
- Young, P. J., Archibald, A. T., Bowman, K. W., Lamarque, J. F., Naik, V., Stevenson, D. S., et al. (2013). Pre-industrial to end 21st century projections of tropospheric ozone from the atmospheric chemistry and climate model intercomparison project (ACCMIP). *Atmospheric Chemistry and Physics*, *13*(4), 2063–2090. <https://doi.org/10.5194/acp-13-2063-2013>
- Young, P. J., Naik, V., Fiore, A. M., Gaudel, A., Guo, J., Lin, M. Y., et al. (2018). Tropospheric Ozone Assessment Report: Assessment of global-scale model performance for global and regional ozone distributions, variability, and trends. *Elementa-Sci. Anthropol.*, *6*. <https://doi.org/10.1525/elementa.265>
- Zanis, P., Akritidis, D., Turnock, S., Naik, V., Szopa, S., Georgoulas, A. K., et al. (2022). Climate change penalty and benefit on surface ozone: A global perspective based on CMIP6 earth system models. *Environmental Research Letters*, *17*(2), 024014. <https://doi.org/10.1088/1748-9326/ac4a34>
- Zhang, J., Gao, Y., Luo, K., Leung, L. R., Zhang, Y., Wang, K., & Fan, J. (2018). Impacts of compound extreme weather events on ozone in the present and future. *Atmospheric Chemistry and Physics*, *18*(13), 9861–9877. <https://doi.org/10.5194/acp-18-9861-2018>
- Zhang, L., Brook, J. R., & Vet, R. (2002). On ozone dry deposition—With emphasis on non-stomatal uptake and wet canopies. *Atmospheric Environment*, *36*(30), 4787–4799. [https://doi.org/10.1016/S1352-2310\(02\)00567-8](https://doi.org/10.1016/S1352-2310(02)00567-8)
- Zhang, L., Brook, J. R., & Vet, R. (2003). A revised parameterization for gaseous dry deposition in air-quality models. *Atmospheric Chemistry and Physics*, *3*(6), 2067–2082. <https://doi.org/10.5194/acp-3-2067-2003>
- Zhang, S., Fu, H., Wu, L., Li, Y., Wang, H., Zeng, Y., et al. (2020a). Optimizing high-resolution Community Earth System Model on a heterogeneous many-core supercomputing platform. *Geoscientific Model Development*, *13*(10), 4809–4829. <https://doi.org/10.5194/gmd-13-4809-2020>
- Zhang, S., Xu, S., Fu, H., Wu, L., Liu, Z., Gao, Y., et al. (2023). Toward Earth system modeling with resolved clouds and ocean submesoscales on heterogeneous many-core HPCs. *National Science Review*, *10*(6). <https://doi.org/10.1093/nsr/nwad069>
- Zhang, T., de Jong, M. C., Wooster, M. J., Xu, W., & Wang, L. (2020b). Trends in eastern China agricultural fire emissions derived from a combination of geostationary (Himawari) and polar (VIIRS) orbiter fire radiative power products. *Atmospheric Chemistry and Physics*, *20*(17), 10687–10705. <https://doi.org/10.5194/acp-20-10687-2020>
- Zheng, B., Cheng, J., Geng, G., Wang, X., Li, M., Shi, Q., et al. (2021). Mapping anthropogenic emissions in China at 1 km spatial resolution and its application in air quality modeling. *Scientific Bulletin*, *66*(6), 612–620. <https://doi.org/10.1016/j.scib.2020.12.008>

References From the Supporting Information

- Flemming, J., Huijnen, V., Arteta, J., et al. (2015). Tropospheric chemistry in the Integrated Forecasting System of ECMWF. *Geoscientific Model Development*, *8*(4), 975–1003. <https://doi.org/10.5194/gmd-8-975-2015>